5-2019

Development of Flexible Photo-Mechanoluminescent Polymeric Based Systems

Carlos Hernandez
The University of Texas Rio Grande Valley

DEVELOPMENT OF FLEXIBLE PHOTO-MECHANOLUMINESCENT POLYMERIC BASED SYSTEMS

A Thesis

by

CARLOS HERNANDEZ

Submitted to the Graduate College of
The University of Texas Rio Grande Valley
In partial fulfillment of the requirements for the degree of

MASTER OF SCIENCE ENGINEERING

May 2019

Major Subject: Mechanical Engineering

DEVELOPMENT OF FLEXIBLE PHOTO-MECHANOLUMINESCENT

POLYMERIC BASED SYSTEMS

A Thesis
by
CARLOS HERNANDEZ

COMMITTEE MEMBERS

Dr. Karen Lozano
Chair of Committee

Dr. Javier Ortega
Committee Member

Dr. Rogelio Benitez
Committee Member

May 2019

ABSTRACT

Hernandez, Carlos, Development of Flexible Photo-Mechanoluminescent Polymeric Based Systems. Master of Science Engineering (MSE), May, 2019, 83 pp., 10 tables, 73 figures, references, 60 titles.

The project focuses on the creation of nanofiber systems with enhanced photo-mechanoluminescent response and high mechanical flexibility to further enhance promising optical applications. Lanthanide-Polyvinyl Di-Fluoride fiber systems were created using centrifugal spinning and characterized using SEM, FTIR, XPS, DSC, and PL. Fibers luminescence response was gotten when induced by ultraviolet light and the application of an impact force.

DEDICATION

I want to dedicate this work to God, he who has always been by my side in troubled times and has never given up on me. My dad, Raul Hernandez, whose work and dedication led me to achieve my career. My mother, Ma. Elvira Lopez, whose love and comfort motivated me to go forward. My brothers, Itzel and Jose Raul, whose life examples made me the person I am today. My nephews, Raulito and Gio, that teach me what unconditional love is. And finally, my grandmother, Josefina Portilla, that will forever and always be in my heart. I hope for one day to have the opportunity to reward their love and support.

ACKNOWLEDGEMENTS

I would like to give my most sincere gratitude to Dr. Karen Lozano, whom without her guidance and support, this project wouldn't have been accomplished. Her ability to help students on academic and personal issues is beyond imagination. I consider it a privilege to have worked under her supervision and will always cherish the moments I spent on the lab.

I would like to thank Dr. Javier Ortega and Dr. Rogelio Benitez for their academic and moral support throughout my thesis project, Homero Gonzalez and Omar Torres for their mentorship and advice, and Jose Zuniga and Victoria Padilla for their aid in data facilitation and companionship. I want to give a special thanks to my lab partners and friends, Misael, Rodolfo, Raul, Ydana, Dulce, Rene, Jorge, Eric, Lilian, and Hector for making these past two years the best in my life. This project is supported by NSF PREM award under grant No. DMR-1523577: UTRGV-UMN Partnership for Fostering Innovation by Bridging Excellence in Research and Student Success.

TABLE OF CONTENTS

Page

LIST OF TABLES

Page

LIST OF FIGURES

Page

CHAPTER I

INTRODUCTION

Crack detection is a critical point in minimizing the outcome of a fracture in a component or infrastructure system. In such occurrences, crack detection/monitoring systems are implemented to reveal the presence or growth of a solid discontinuity using imaging techniques, such as ultrasonic or vibrational. These types of discontinuities occur and propagate due to a mechanical effort within or on the surface of the material. The mechanical force applied to the specimen can range from pressurized to vibrational force; including tensile, shear, and compressional forces [2,3]. Due to the potential causes of crack propagation, photo-mechanoluminescence can be a possible solution to the detection of this incident [1-3].

The absorption of light to produce light emissions on a material is called photoluminescence (PL). This technique applies photons to excite the outer electrons of an element. The electrons make a transition from the ground state to the lowest unoccupied molecular orbital; this change in energy creates light emissions on photoluminescence systems. On another instance, mechanoluminescence (ML) is a compelling research topic in academia due to its happenstance. An amalgamation of Latin and English words, the "mechano-" term is defined as to the exertion of a mechanical force into a material to generate "luminescence," or light emission. The electrical discharge between the solid faces creates the luminescence in mechanoluminescent systems [4-7]. Therefore, it is theorized that most ML materials are

piezoelectric by nature. On smart polymer materials, electroactive phases could assist in the deliverance of mechanoluminescence emissions.

The use of polyvinyl difluoride (PVDF) has been previously studied for its piezoelectric applications, for example in triboelectric nanogenerators and in flexible device applications. This property is attributed to the presence of the β phase, that provides PVDF with the highest dielectric constant among polymers as well as high-level of electroactive response. Dynamic-mechanical properties, such as low density, high strength, and high flexibility, makes PVDF a material suitable to be applied as a polymer matrix [8-10].

Lanthanides are rare-earth elements commonly used for luminescence applications due to their f-f transition. This transition enables the lanthanide elements to emit high-quality colors from the visible to the near-infrared spectrum. Europium, for instance, is used as a red phosphor on television appliances due to its luminescence properties. Cerium is also used for optical applications since it scintillates under ultraviolet light. Despite the lanthanides optical properties, both lack mechanical strength and processability [9, 11, 12].

The motivation of this project is to create flexible photo-mechanoluminescent polymeric based systems based on nonwoven nanofiber mats developed through the Forcespinning® technology. These flexible ML mats were analyzed based on applied forces and corresponding light emission.

CHAPTER II

THEORETICAL BACKGROUND

2.1 Photo-Mechanoluminescence Properties on Polymeric Nanofibers and their Dopant Agents

The following sections depict background from related scientific studies correlated to polymeric nanofibers with luminescent attributes. Mention of useful materials to produce mechanoluminescence and photoluminescence are discussed, as well as experimental procedures and characterization methods to perform and calculate such occurrence.

2.2 Luminescence Systems

2.2.1 Mechanoluminescence

The first recorded mechanoluminescence appearance was in 1605, by Francis Bacon. According to the story, light emission happened due to the breakage of sugar crystals [4]. As stated by Bünzli, the term Mechanoluminescence (ML) is defined as the emission of light imposed by a mechanical force on a material. ML occurrence is dependent upon two things [5]:

1. The type of mechanical energy applied: rubbing, scratching, hitting, etc.
2. The morphology and purity of the material.

Compression of materials can create ML, such as in the study *Development of elastico-luminescent nanoparticles and their applications*, where Xu, *et. al.*, tested elastic-luminescent nanoparticles to check its mechanoluminescence intensity [12]. The nanoparticles, $SrAl_2O_4$:Eu, were developed at the National Institute of Advanced Industrial Science and Technology (AIST). An ultrasonic spray process was used to prepare the samples with a particle size from 0.1-1 µm. Characterization methods included x-ray diffraction (XRD) and excitation/emission spectra. The nanoparticles were homogenized into an epoxy film, and the ML intensity was analyzed under a compression load, as portrayed in Fig. 1. The nanoparticles were encased on an epoxy resin and made into a cylindrical rod, where torsional forces were applied, and a luminescence change was noted.

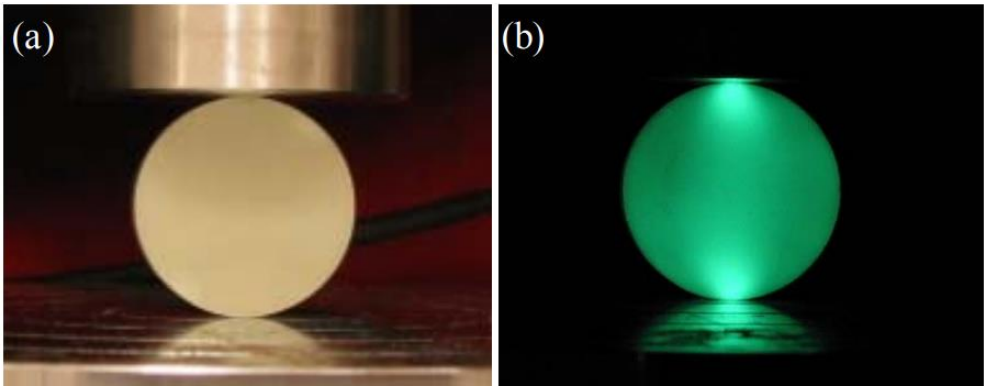

Fig. 1. SAO/Epoxy film (a) before compression; (b) under compression [4].

2.2.2 Mechanoluminescence Term Description

According to Bünzli, *et al.*, mechanoluminescence is an agglomeration of different mechanical concepts [4]. Such contents contain “piezo, tribo, stress,fracto, plastico, elastico, cutting, cleaving, grinding, rubbing, compressing, and crushing.” In *An Introduction to Luminescence of Solids*, the author subdivides the concept into six terms, as seen in Table 1:

Term	Light Emission Created by:
Sonoluminescence	Ultrasonic sound waves
Triboluminescence	Friction
Fractoluminescence	Fracture
Piezoluminescence	Pressure
Crystalluminescence	Chemical-induced
Thermoluminescence	Temperature-induced

Table 1. Mechanoluminescence Terms [13]

Table 1 portrays the subdivided terms of mechanoluminescence with each of the causes [13].

Piezoluminescence happens when pressure is applied to a material, and it creates light emissions, as seen in Fig. 2 [14]. According to the *Piezoluminescence phenomenon*, a scientific article by the Physics Department from Kuwait University, this phenomenon is explained as "recombination processes involving electrons, holes and impurity ion centers" [14]. The materials that show piezoluminescence the most are irradiated salts, such as NaCl, KCl, KBr. Also, Owsley Stanley, an audio engineer and chemist/producer in the early history of lysergic acid diethylamide (LSD), discovered the piezoluminescence properties of N,N-Dimethyltryptamine, 5-methoxy-N,N-dimethyltryptamine, and LSD [15].

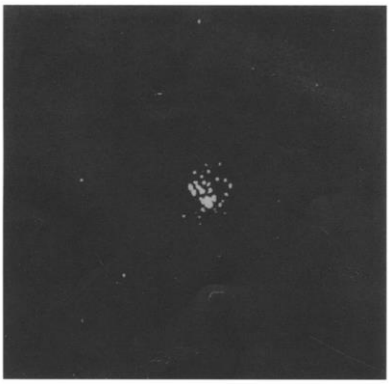

Fig. 2. Photograph from a quartz being impacted and showing piezoluminescence [16].

Triboluminescence is commonly present in minerals like quartz, common opal, calcite, and feldspar. Is widely theorized that 50% of the mentioned crystalline materials exhibit triboluminescence. Quartz shows high triboluminescence properties when two parts collide with each other, creating fracture or friction. Triboluminescence is the most common type of mechanoluminescence, as being one of the best methods to obtain luminescence due to its testing and material abundance. Triboluminescence cannot be categorized as a substantial property since the property varies from each material sample [13].

Crystalloluminescence is the occurrence when a concentrated solution undergoes a crystal transformation like solidification, and on some occasions, when the material/solution melts. In crystalloluminescence, mechanical stresses that produce the growth or regression of crystals lead to fluorescence. Barium or strontium bromates, as well as N- isopropylcarbazole, are good examples of crystalloluminescence [13].

2.2.3 Mechanoluminescence Crystal Structures

According to Zink, *et al.*, in *Squeezing Light out of Crystals: Triboluminescence*, for specimens to exhibit light under mechanical excitations the samples need to have polar crystallographic groups [17]. Furthermore, the intensity of mechanoluminescence can increase when the sample structure is not aligned correctly (due to impurities or disorder) or when the crystals are non-centrosymmetric. Lanthanide-salts crystals are suitable due to their dissymmetry [18].

2.2.4 Mechanoluminescence Testing Procedures

Measuring mechanoluminescence requires the use of two components:

1. Instrumentation in-charge of exerting the mechanical force into the sample.
2. A light measuring device in charge of recording the luminescence intensity of the sample.

Fig. 3. shows a torsional system to calculate the mechanoluminescence intensity on a sample road.

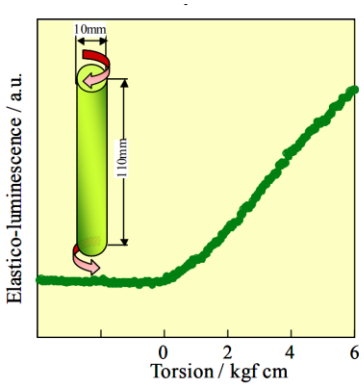

Fig. 3. The luminescence intensity of the testing sample under torsional forces [12].

According to Xu, the sample tested was a europium-doped strontium aluminate (SAO) nanoparticles injected into an epoxy film. The film was tested under torsional forces and the luminescence was recorded [12].

On the *Ball impact induced elastic-mechanoluminescence for impact sensor*, Jha*, et al.*, portrays another standard testing procedure to check for ML [19]. Jha prepared phosphor composite film made out of Sr0.97Al2O4:Eu0.01, Dy0.02 and polycarbonate resin. The experimental setup included a 1- PVC pipe, 2- steel ball, 3- mechanoluminescent film, 4 - photomultiplier tube, 5 - stand, 6 - sample holder, 7 - wooden block and 8 - iron base mounted on a table as portrayed in Fig. 4.

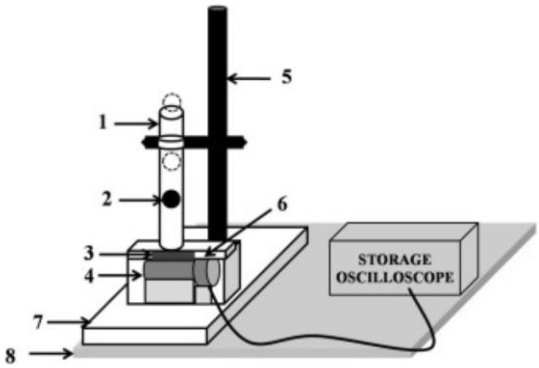

Fig. 4. ML experimental set up for films [19].

The experiment starts with a steel ball entering the PVC pipe. Then the steel ball travels downward and hits the ML film. The photomultiplier detects the signal and sends the data into the storage oscilloscope. The film-sample mounting is shown in Fig. 5.

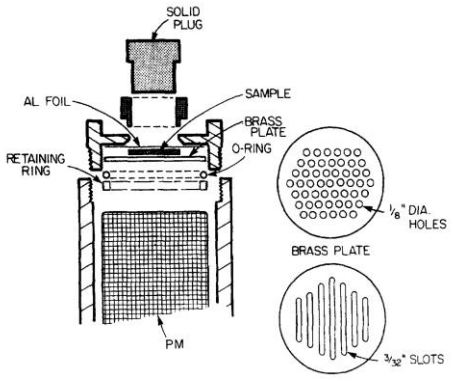

Fig. 5. Sample mounting for photomultiplier recording for piezoluminescence [19].

The ML film is placed above the photomultiplier tube. The tube records the luminescence intensity and sends the data to the oscilloscope. Data presented on the oscilloscope is shown in Fig. 6.

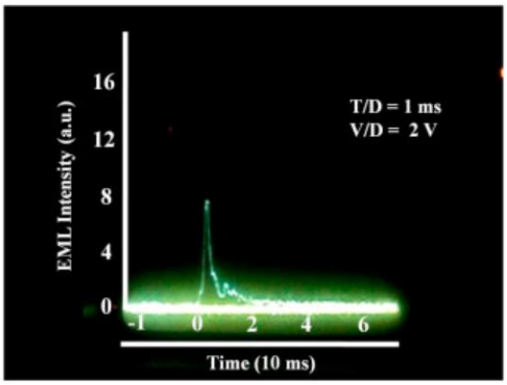

Fig. 6. ML intensity of $Sr_{0.97}Al_2O_4:Eu_{0.01}$, $Dy_{0.02}$ film shown in milliseconds [19].

Fig.6 shows the luminescence intensity of the film after being impacted by the steel ball. The visible intensity is recorded in milliseconds. Photoluminescence is another luminescence system and is described in the next section.

2.2.5 Photoluminescence

The term photoluminescence is a union of the Latin word -*luminescence,* and the Greek term *photo-*, meaning light. According to *An introduction to luminescence of solids*, Leverenz, *et al.*, states that any emission of light on a solid created by the absorption of light is called photoluminescence [20].

In *Optical Properties of Semiconductor Nanowires: Insights into Band Structure and Carrier Dynamics,* in *Semiconductors and Semimetals,* Jackson, *et al.*, explains the photoluminescence intensity as being categorized by energy transitions [21]. The emitting state of a material is the measured absoprtion strength when the electrons are excited. The excitation energy varies depending on the element, this is proper to the different electronic transitions.

2.2.6 Photoluminescence Electronic Transitions

In *Chemi Oberstufe,* Arnold, *et al.*, explains that light emissions are generated due to electronic transitions within the photoluminescenct material [6]. Fig. 7, below portrays an example of excited electronic transitions.

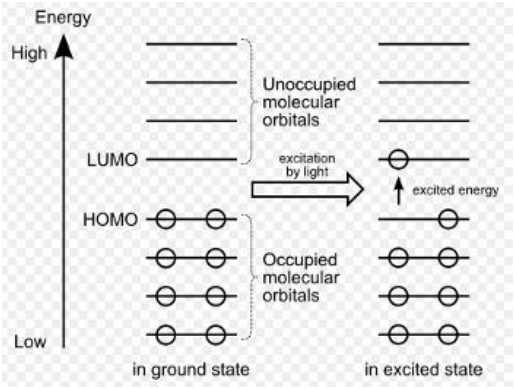

Fig. 7. Schematic of electronic transitions being excited [6].

The photoluminescence process can be explained using Fig. 7. The specimen is at the ground state when no external excitation energy is applied. All the electrons are in the highest

occupied molecular orbital (HOMO). When the material is excited by photons, electrons are excited and move to the lowest unoccupied molecular orbital (HUBO). When the electrons return to the HOMO, a photon is radiated, creating light emission [7].

2.2.7 Photoluminescence Instrumentation

Harris, *et al.*, in *Quantitative Chemical analysis*, explains the use of photoluminescence equipment, as depicted in Fig. 8.

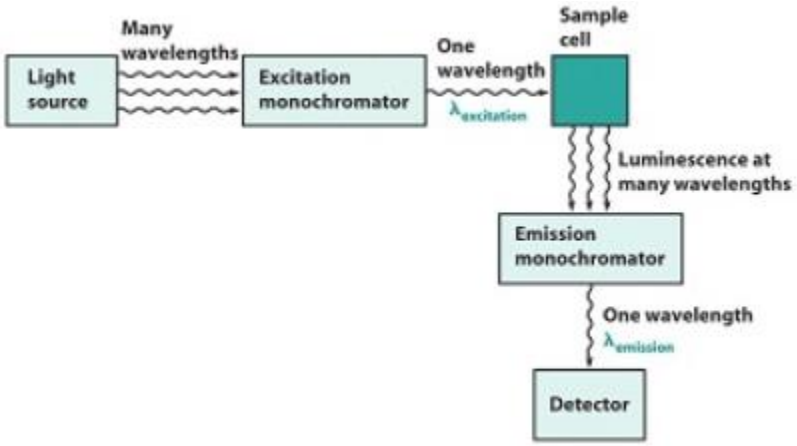

Fig. 8. Photoluminescence Instrumentation Schematic[22]

The light source provides the excitation energy, and the excitation monochromator narrows the wavelengths into one single excitation wavelength. The sample is excited to a specific wavelength and emits light. The emission monochromator constrains the wavelength into a single band, that is transmitted to the detector [22-24].

2.2.8 Photo-Mechanoluminescence

In *Lanthanide Mechanoluminescence*, Bünzli, *et al.*, mentions the occurrence of mechanoluminescence on europium phosphate sample while being excited with UV light [4]. Furthermore, in the *Development of new elasticoluminescent material SrMg2(PO4)2:Eu*, Kamimura describes the use of photoluminescence as a mechanical force is applied [25]. An example is provided in Fig. 9.

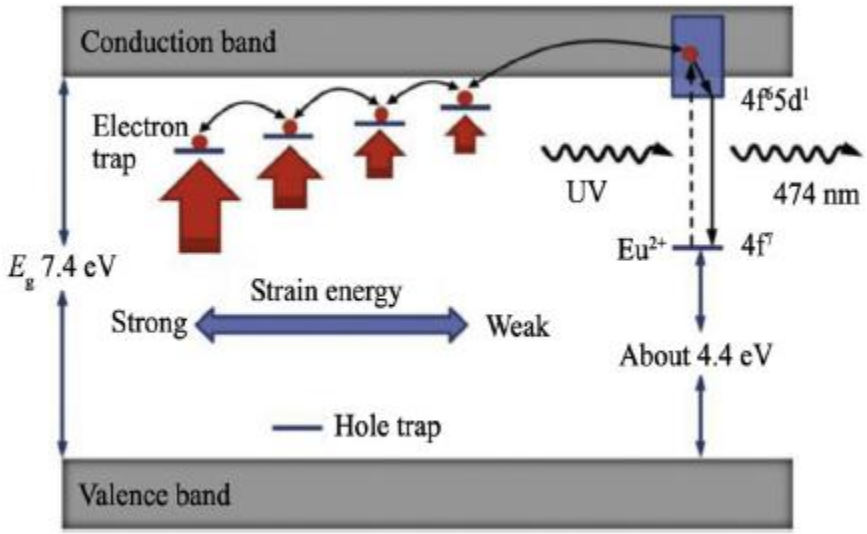

Fig. 9. Photo-Mechanoluminescence Schematic Diagram [4].

Fig. 9 portrays the schematic diagram of a photo-mechanoluminescence system. A europium (Eu) phosphate sample is tested. Its 4f electronic transitions characterize the lanthanide. First, Eu^{2+} is at the ground state and in the valence band. Ultraviolet light is irradiated onto the sample, eliminating the oxygen and creating vacancies. The europium electrons are excited and enter the conduction band. The electrons are trapped in the oxygen vacancies. When a mechanical force is applied, the structure is deformed, and the trapped electrons are freed. These electrons join their lanthanide-luminescent center (Eu^{+2}) and emit a change in luminescence [4, 25, 26].

2.2.9 Photo-Mechanoluminescence Instrumentation

In *Optical Pressure Sensor Based on the Emission and Excitation Band Width (fwhm) and Luminescence Shift of Ce3+-Doped Fluorapatite—High-Pressure Sensing*, Runowski, *et al.*, tested the luminescence of a cerium-lanthanide sample as pressure was excited [27]. The paper reports the use of photoluminescence equipment, mentioned in section **2.2.2b Photoluminescence Instrumentation**, and a diamond anvil cell (DAC). Fig. 10 depicts a DAC instrument.

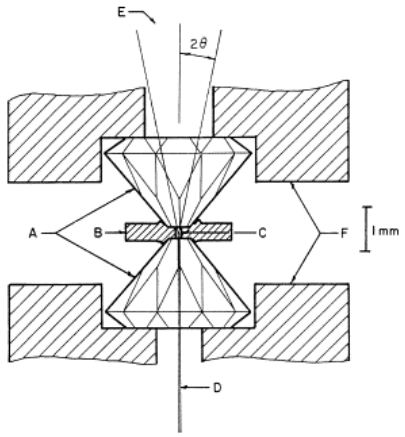

Fig. 10. Diamond anvil cell schematic [28].

Fig. 10 portrays the schematic of the diamond anvil cell, where point A shows the diamonds, B the gaskets, C the pressure chamber, F the diamonds' plate, and points E and D depict the path of the photons [28]. The diamonds are the components that provide the pressure in the system. The sample is assembled between the gaskets. The indentation of the diamonds on the gaskets creates the pressure required. The light source passes through the top diamond, travels through the sample, and exits the bottom diamond. The photons released are transmitted to the detector.

As the pressure is induced into the system, the wavelength of certain lanthanide materials changes, such as cerium and europium lanthanides.

2.3 Material Selection

Europium and cerium lanthanides were selected based on their potential to enhance luminescence properties on simple materials. Despite its luminescence properties, the lanthanides lack mechanical strength, thermal stability, and have low manufacturing processability [11]. Previous studies show lanthanide complexes processed into polymer matrixes [9, 12]. The chosen polymer matrix was polyvinylidene fluoride (PVDF) due to its high strength, toughness, and piezoelectric characteristics to enable luminescence; as well as its easy of processability to produce nanofibers.

2.3.1 Europium and Cerium Lanthanides

According to *Lanthanide Mechanoluminescence*, Bünzli, *et al.*, studies the use of lanthanides for force induced luminescence [4]. In the report, the author mentions the application of cerium and europium; the last one mentioned in 80% of lanthanide luminescence scientific reports [4]. Several salts of lanthanides have been studied before, such as nitrates and sulfates [29]. Depending on the type of lanthanide, the distinct the luminous intensity. Europium, for instance, is UV irradiated to test the luminescence intensity as mechanical force is applied [30-32]. Cerium luminescence characteristics make it suitable for optical applications [10].

2.3.2 Europium and Cerium Electronic Transitions

The advantage of cerium, $Ce^{+3,+4}$, and europium ions, Eu^{+3}, has been widely investigated due to their luminescence peaks. Furthermore, under UV excitation, the lanthanides show emission peaks in visible and infrared spectrum. The symmetry of the crystal structure and the electronic transitions produce and affect the light emission [11, 33-36].

Depending on the change in symmetry of lanthanide ions, defines the interchange of electronic transitions. Formation of cracks or impurities inside the microcrystal makes it difficult

to illustrate the crystal symmetry; however, this reveals the change in intensity [34]. The crystal dislocations interact with the f-centers of the lanthanides. The electrons encounter impurity centers, such as oxygen vacancies, and are captured. When the electrons are excited, they recombine with their element and create light emission [4].

When excited by ultraviolet light (UV), the lanthanide experience *d* to *f* electronic transitions. Cerium, for instance, experiences $^5D_0 \rightarrow {}^4F_1$ generating blue-light emissions. For europium complexes, the electric dipole transition $^5D_0 \rightarrow {}^7F_2$ creates red-light fluorescence [10, 11, 33, 34, 37].

2.3.3 Europium and Cerium Luminescence Applications

Besides potential removal of carbon emissions and wastewater purification applications, cerium has been widely used for its optical applications. For instance, cerium complexes have been used in laser-light emitting diodes, photo-detectors and optical wave detectors [38-41]. Europium spectroscopic properties make it also suitable for luminescence applications. Its red-light emission is applied in LEDs and full-color displays, while it also can be used in gas sensors [33].

Implementing a polymer matrix benefits the lanthanide emission by immobilizing the lanthanide particles, as seen in Fig. 11 [33].

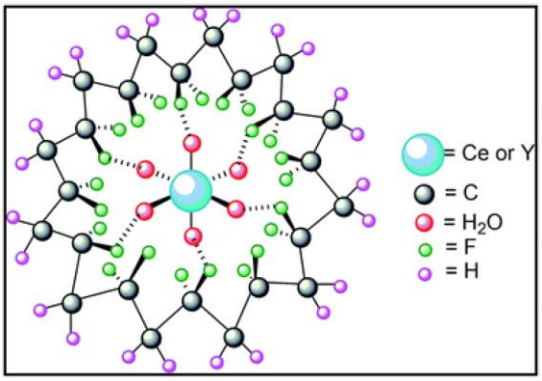

Fig. 11. Schematic of cerium (Ce) or yttrium (Y) doped in a polymer matrix [9].

Fig. 11 illustrates polyvinylidene fluoride (PVDF) doped with yttrium or cerium elements. The schematic shows cerium nitrate attached to the fluoride molecules of the PVDF to enhance the β-phase [9].

2.3.4 Polyvinylidene Difluoride (PVDF) Polymer

Polyvinylidene difluoride (PVDF) properties include high piezoelectric response, flexibility, and chemical resistance. Consequently, PVDF has been employed in sensors, actuators, and energy harvesting applications [9, 10, 42].

2.3.5 PVDF Polymeric Structure

Fig. 12 portrays the semi-crystalline polymer PVDF with its chemical structure and atomic orientations.

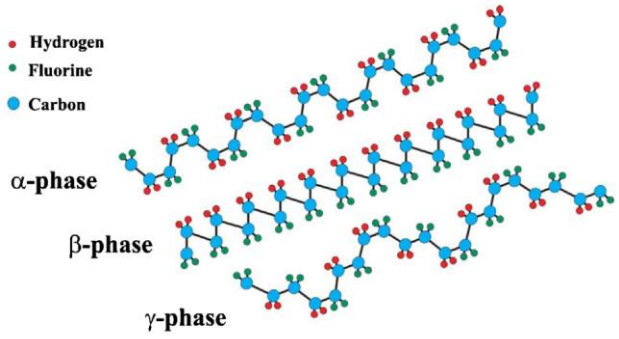

Fig. 12. PVDF chemical structure [8].

According to Martins, *et al.*, hydrogen, fluorine and carbon atoms constitute the PVDF chemical structure [8]. The figure also depicts the polymorph phases: α, β, γ.

The non-polar α-phase has an orientation of TGTG' and corresponds to the thermal stability of the polymer. The γ-phase occurs when the polymer is melt crystallized and has an orientation of TTTGTTTG'. The β-phase is identified as the polar or electroactive phase of the polymer and characterized by the asymmetric alignment of -CF2 and -CH2 (TTTT). This orientation makes it easier for the polymer to attract electrons easily [9, 10, 43].

The β-phase promotes a stronger electrical dipole moment, making it the best piezoelectric polymer [8]. The amount of crystallinity degree and the amount of β-phase content control the piezoelectric performance of the polymer. Also, the elongation of the polymeric structure and the addition of doping agents, such as lanthanides, nanoparticles, or nanofillers, could provide a higher beta phase [8, 10, 42].

2.3.6 PVDF Applications & Processes

PVDF, a semicrystalline polymer, has a high beta phase and a strong resistance to UV radiation and chemicals, making the polymer a widely explored subject in academia. The potential applications range from health monitoring to crack detection devices. For instance, the piezoelectric and mechanical properties make the polymer a suitable candidate for energy harvesting with the use of mechanical force [11, 42, 44].

PVDF is a cost-friendly pressure sensor. For instance, in *Pressure sensor from a PVDF film*, Shirinov, *et al.*, manufactured and tested the output response according to the input pressure and its aging process. The pressure exerted into the PVDF film creates an electrical discharge that is transmitted with the help of the electrode. The PVDF pressure sensor was tested for its voltage capacity, ambient sensitivity, and response time. PVDF exhibited an excellent measurement accuracy and a response time of fewer than 100 microseconds [45].

A film, according to Yokoyama, *et al.*, in *Magneto-impedance properties of thin-film type sensors using CoNbZr/SiO2 multilayer films*, is a thin layer of material. In some applications, films are stacked up to enhance specific properties. For example, Yokoyama makes thin layer films to check the impedance change according to the film layers (thickness). Multilayer films had a high-frequency permeability in comparison with a single layer; the voltage response improved from 140% to 280% [46].

The use of doping agents can enhance the piezoelectric response of the polymer. In *Enhancement of Electroactive β-phase and Superior Dielectric Properties in Cerium Based Poly(vinylidene fluoride)*, Garain studies the use of PVDF with cerium ammonium sulfate (CAS) for its piezoelectric response. In the study, the author uses different concentrations of CAS with PVDF and processes them into films [10].

PVDF can also be processed into fibers. On *Droplet-jet shape parameters predict electrospun polymer nanofiber diameter*, Liu, *et al.*, examines the use of graphene as a doping agent to increase the voltage potential of PVDF nanofibers. On another instance, Tang explores the use of a PVDF film for space exploration, where he uses the piezoelectric sensor to detect the debris collision impact on a spacecraft [42, 47, 48].

PVDF can absorb visible and ultraviolet light, making the polymer resistant to UV light and suitable for luminescence systems. Luminescence properties have further been examined using PVDF films applications. In *Role of Cerium (III)/Yttrium (III) nitrate hexahydrate salt on electroactive β phase nucleation and dielectric properties of poly(vinylidene fluoride) thin films*, Thakur, *et al.*, studies the production of polyvinylidene difluoride (PVDF) films doped with cerium(III)/yttrium(III) salts for luminescence properties. The investigators studied ways to improve the β phase of the polymer while using doping agents, such as graphene, inorganic salts, and metal nanoparticles [9, 49, 50].

PVDF has been previously used to produce nanofibers via the use of electrospinning. Furthermore, in *Red-light-emitting polymer composite based on PVDF membranes and Europium phosphor using Buriti Oil as plasticizer*, Bispo, *et al.*, uses a mixture of the polymer and the europium lanthanide to check the elastic mechanical properties of PVDF and the luminescence properties of the lanthanide [11, 33].

In *Photoluminescent electrospun europium complex Eu(TTA)3phen embedded polymer blends nanofibers*, Dandekar, *et al.*, explored the use of the polymer and the europium lanthanide in fiber systems. With the addition of PVDF, the combined system improves in mechanical properties such as flexibility and thermal stability. The lanthanide experiences a transition of $^{5}D_{0}$ to $^{7}F_{2}$ on the Eu^{+3} ions; the material experiences a higher fluorescent intensity [11].

2.3.7 Polymer and Lanthanides Characterization Techniques

Garain, *et al.*, in *Enhancement of Electroactive β-phase and Superior Dielectric Properties in Cerium Based Poly(vinylidene fluoride)*, uses FTIR to study the PVDF polymorphs phases, as seen in Fig. 13 [10].

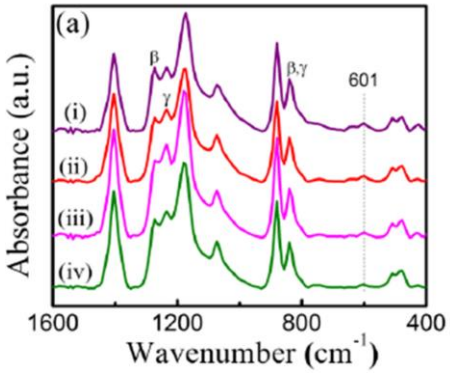

Fig. 13. FTIR spectra of PVDF doped with cerium [10].

Fig. 13 shows PVDF doped with 0.5% (i), 0.25 (ii), 0.125 (iii) and 0.062 (iv) cerium. The significance of Fig. 13. is the peak at 1276 cm-1. The characteristic vibration bands for the B and gamma phases are at 840 and 510 cm-1 [10].

In *Photoluminescent electrospun europium complex Eu(TTA)3phen embedded polymer blends nanofibers*, Dandekar, *et al.*, uses a scanning electron microscope (SEM) to check the fiber diameter of PVDF and polystyrene (PS) nanofibers [11].

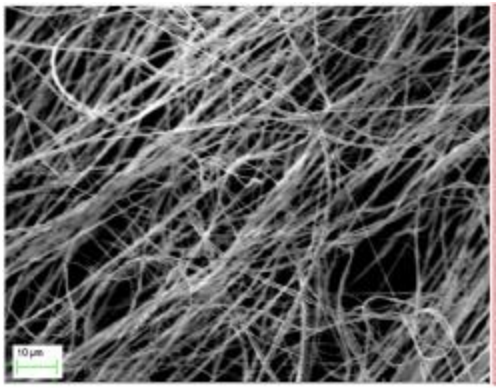

Fig. 14. SEM image of PVDF-PS nanofibers [51].

Fig. 14 shows the SEM image of electrospinning nanofibers.

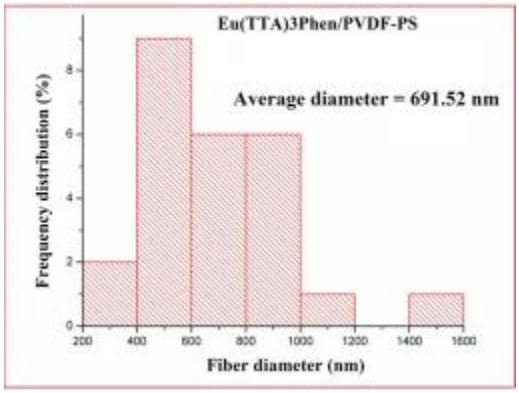

Fig. 15. PVDF-PS fiber diameter distribution [51].

Fig. 15 demonstrates the bell curve distribution of the fibers. It was found that the fibers had an average diameter of 691.52 nm [51].

On *Role of Cerium (III)/Yttrium (III) nitrate hexahydrate salt on electroactive β phase nucleation and dielectric properties of poly(vinylidene fluoride) thin films,* Thakur, *et. al.*, uses differential scanning calorimetry to check the PVDF behavior with the addition of cerium lanthanide [9].

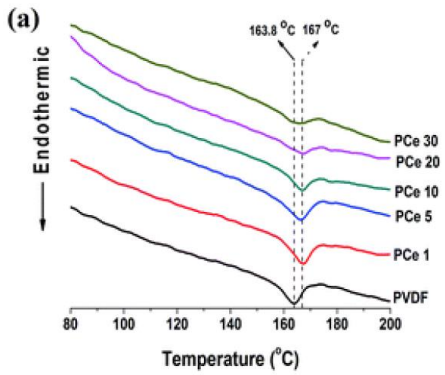

Fig. 16. DSC thermograph of pure PVDF films doped with cerium [9].

Fig. 16 portrays the use of DSC being implemented to verify the different crystalline phases of the polymer. PVDF has a melting peak at 163.8 °C; this peak corresponds to the crystallization phase of α. With the increase of the β phase by the addition of the cerium nitrate, the melting temperature shifted by 3.2-3.8 °C.

In *Photoluminescent electrospun europium complex Eu(TTA)3phen embedded polymer blends nanofibers*, Dandekar, *et al.*, checks the photoluminescent intensity of the europium lanthanide, as seen in Fig. 17 [11].

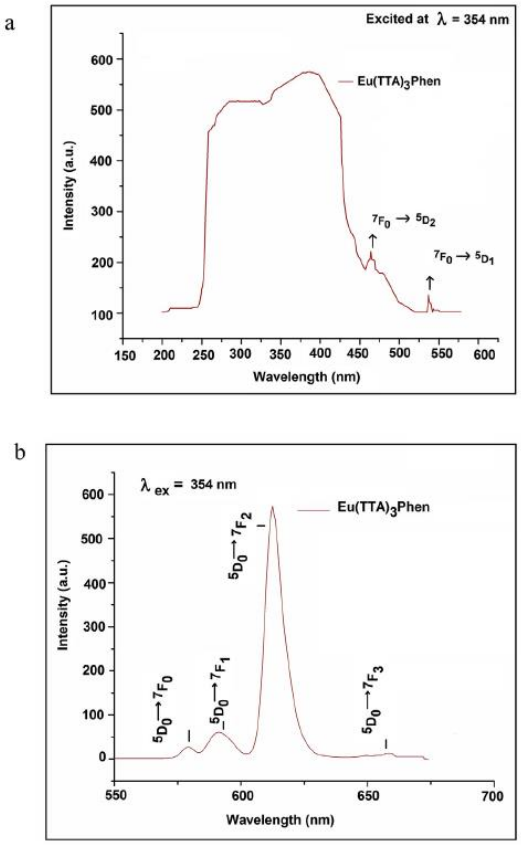

Fig. 17. Excitation (a) and Emission (b) of Eu(TTA)$_3$phen [11].

In Fig. 17(a) the excitation spectrum was set at 615 nm, where it exhibits broadband from 250 to 400 nm, this is due to the electron transition of the ligands demonstrating the energy transfer occurs from the Eu(III) ions. In Fig. 17(b) the excitation was set at 354 nm, and the testing parameter was set from 550 to 700 nm range. The sample showed peaks at 580, 593, and 613 nm. At 580 nm, the emission corresponds to the transition of $^5D_0 \rightarrow ^7F_0$ and has a low intensity due by the "selection of forced dipole transitions." At 593 nm, the emission band corresponds to the $^5D_0 \rightarrow ^7F_1$ magnetic transition; it also portrays a low intensity. At 613 nm

shows the highest emission (electric dipole), the emission band corresponds to the $^5D_0 \rightarrow ^7F_2$ hypersensitive transition. This emission is the one responsible for the red luminescence of the europium complex. The author also uses the International Lighting Commission (CIE) graph, as portrayed in Fig. 18 [11].

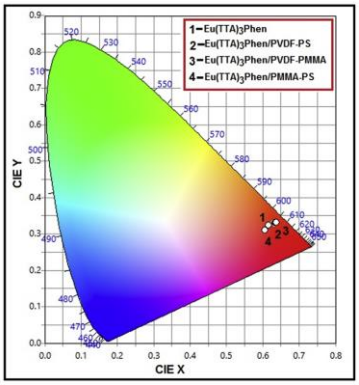

Fig. 18. The chromaticity of Eu(TTA)$_3$phen bulk and its polymer blends [22].

The International Commission on Illumination (CIE) chromaticity coordinates of Eu(TTA)$_3$phen and its polymers blends are graphed according to the photoluminescence spectra. The standard value of red chromaticity set by the National Television Standard Committee (NTSC) for x is 0.68 ad for y is 0.32. Bulk europium got values at 0.61 and 0.32, while the polymer blends PVDF-PS and PVDF-PMMA got x = 0.64, y = 0.33 and x = 0.64, y = 0.34, respectively [11].

2.4 Forcespinning Technology

Electrospinning has long been used to create polymeric nanofibers; nevertheless, in *Electrospinning to Forcespinning*, Sarkar, *et al.*, explains a different approach to create nanofibers, called Forcespinning. On Forcespinning method, the production rate was improved while a low fiber diameter was produced. Use of several spinning attachments, called spinnerets, can be used to produce nanofibers. The spinneret configuration, rheological properties of the solutions, the rotational speed, and ambient temperature can affect the fiber diameter of the polymer solution. In the end, the Forcespinning® method was theorized to provide a low cost-mass production nanofiber method for polymeric solutions [52]. To explain electrospinning, Fig. 19 portrays a typical electrospinning setup [48].

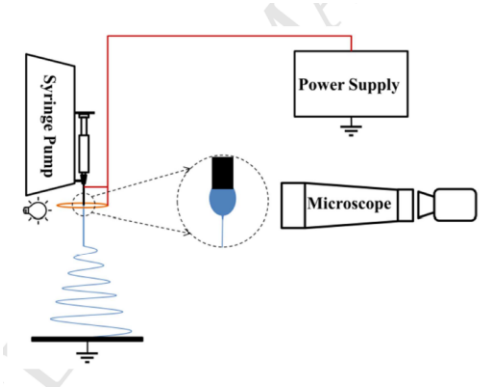

Fig. 19. Experimental setup of electrospinning [42].

In electrospinning an electric field is applied to the solution exiting the syringe. The syringe releases the polymer nanofibers. Electrospinning has a low production rate, requires the use of certain dielectric properties and often the use of toxic organic solvents [48, 52].

Forcespinning is explained in *Production of carbon fibers through Forcespinning® for use as anode materials in sodium ion batteries*, where Flores explains the use of Forcespinning® technology to produce carbon fibers. Forcespininning® technology involves the use of centrifugal forces on polymer solutions to overcome the surface tensions, for it to exit the

spinneret arms and produce the nanofibers. The Forcespinning® machine runs could run up to speeds of 20,000 RPMs. The use of such technology is a safer alternative than electrospinning, due to its fiber production without the use of high voltages. Fig. 20 shows the use of Forcespinning® technology [51].

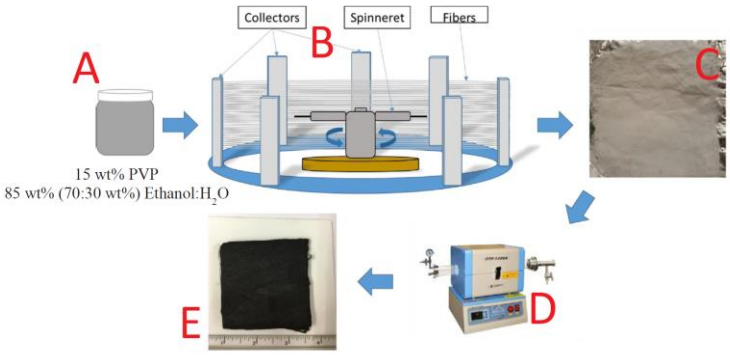

Fig. 20. Schematic of the PVP-carbon nanofiber production using Forcespinning® Tech. [43].

Fig. 20 shows the use of Forcespinning® technology. Fig. 20 (A) shows a PVP solution made from PVP, ethanol, and water. 20 (C) portrays a polymer mat made from Forcespinning® technology. Fig. 20 (D) shows the nanofibers dried on the vacuum oven. Fig. 20 (E) shows that the carbon nanofibers produced [51].

2.5 Motivation

The motivation of this project is to produce flexible PVDF fibers doped with europium and cerium lanthanides using the Forcespinning® method. As a mechanical force is induced into the polymeric-lanthanide systems, a change in luminescence is anticipated. As per our knowledge, no PVDF-lanthanide fibers have been produced using centrifugal spinning; nonetheless, used for pressure induced luminescence. Characterization methods have been implemented. Scanning electron microscope (SEM) was used to analyze the fiber diameter. X-ray photoelectron spectroscopy (XPS) was used to verify the composition of the polymeric-lanthanide fibers. To consider the crystallinity composition, differential scanning calorimetry (DSC) was used. The use of Fourier transform infrared spectroscopy (FTIR) was used to quantify the beta phase on the fiber samples. At last, the diamond-anvil cell was used to check the luminescence of the polymeric systems under pressure.

CHAPTER III

EXPERIMENTAL TECHNIQUES

The necessary equipment, machinery and characterization apparatus, to produce and analyze the luminescent nanofibers are discussed in the following paragraphs.

3.1 Nanofiber Production and Characterization Techniques

The nanofiber production technique implemented was the Forcespinning®, or centrifugal spinning, method. The use of a magnetic-solution stirrer was used to homogenize the polymeric solution. A Forcespinning® cyclone was the equipment required to produce the nanofibers. A scanning electron microscope (SEM) was used to analyze the fiber diameter. X-ray photoelectron spectroscopy was implemented to verify the composition of the fibers.

3.1.1 Hot Plate Magnetic-Solution Stirrer

A polymer solution consists of the polymer powder and the solvents. With the use of a magnetic-solution stirrer, the powder and the solvents are entirely homogenized. A hot plate magnetic-solution stirrer includes temperature-controlled features and a select range of rpms to mix the polymeric solution, as required thoroughly.

3.1.2 Forcespinning® Cyclone

Forcespinning® technology is a relatively new method to produce nanofibers. As mentioned before, electrospinning has a low nanofiber production rate and is required to run at voltages ranging from 1-50 kV. The use of Forcespinning® cyclone is mentioned in Fig. 21.

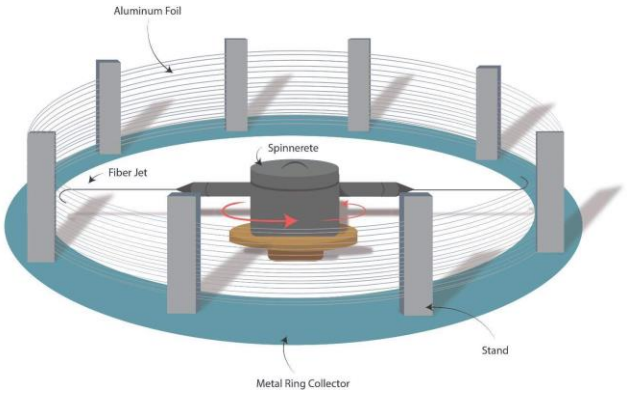

Fig. 21. Forcespinning® nanofiber production method.

Fig. 21 portrays the nanofiber production using the Forcespinning® method. The use of a spinneret, a rotating device attached to a motor, spins at high revolutions up to 20,000 rpms. The centrifugal forces extrude the polymer solution. The solution evaporates and goes from a viscoelastic state to a solid, becoming nanofibers. The Maxwell viscoelastic model could be used to approximate the Forcespinning® method. The nanofibers get stuck in the stands and are collected afterward [52].

3.1.3 Scanning Electron Microscope (SEM)

Scanning electron microscope (SEM) is high-resolution imaging equipment used to analyze the surface morphology of a specimen. Fig. 22 portrays the operation and components on an SEM equipment.

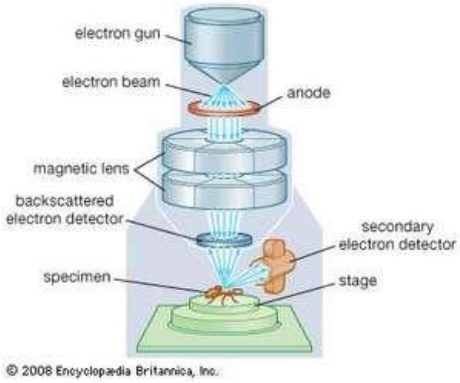

Fig. 22. SEM operation and components [53].

The SEM requires high voltages for the electron gun to produce the stream of electrons or electron beam. The anode attracts the electrons and transmits them into the magnetic lens. The magnetic lens focuses the electrons towards the specimen, where the electron detectors gather the scattered electrons. The interactions between the detectors and a central processing unit (CPU) generate a high-resolution image of the specimen. The generated images can provide insight into the orientation and diameter of fibers [54]. In this work SEM was mostly used to measure the fiber diameter and surface roughness.

3.1.4 X-Ray Photoelectron Spectroscopy (XPS)

The x-ray photoelectron spectroscopy (XPS) technique was used to analyze the composition of the fibers. XPS checks the surface chemical composition of different type of elements due to their electronic structure. Fig. 23 portrays the XPS spectroscopy technique.

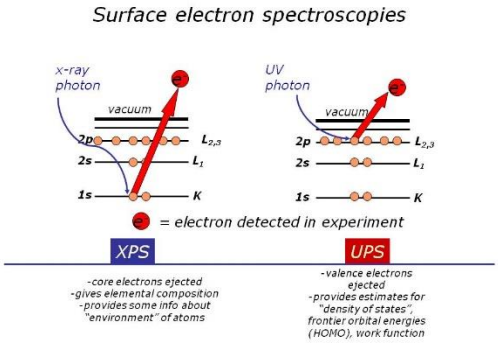

Fig. 23. XPS spectroscopy technique [55].

Fig. 23 shows the x-ray photon from the XPS machine hitting a specimen. The photon hits a core electron, portraying distinctive kinetic energy. The chemical composition is determined from the electronic structure. The advantages of XPS is the information it gives about the sample chemical bonding, and that is a non-destructive technique [55]. The use of the XPS required to verify the chemical composition of the fibers.

3.2 Phase Identification Techniques

Differential scanning calorimetry (DSC) and Fourier transform infrared spectroscopy (FTIR) were implemented to identify the polymorphs phases of the polymer.

3.2.1 Differential Scanning Calorimetry (DSC)

The differential scanning calorimetry (DSC) equipment was utilized in this project to get the phase identification of the semi-crystalline polymer, polyvinylidene fluoride (PVDF). The

DSC analyzes the heat flow measurement of the polymeric sample. The schematic of the system is displayed in Fig. 24.

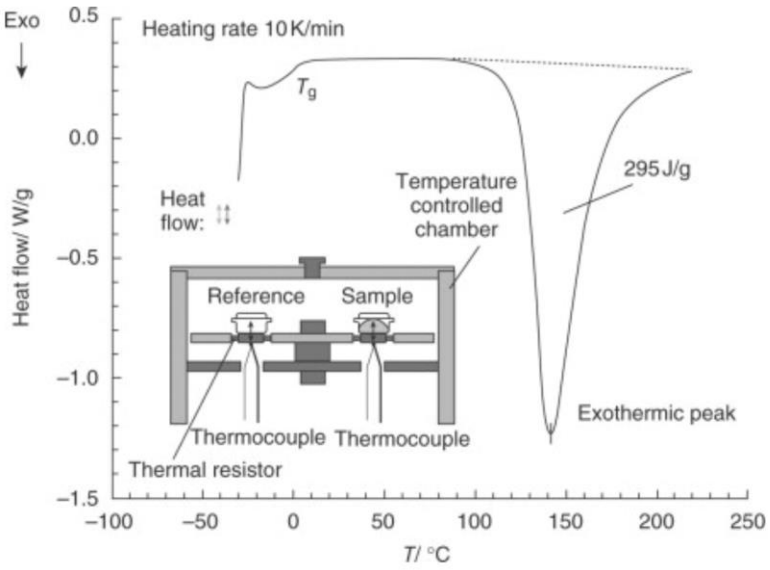

Fig. 24. DSC schematic [56].

The DSC measures the heat flow difference between the sample and the reference. A thermocouple is used to check the temperature of the crucibles, and the thermal resistors regulate the temperature. In polymers, DSC can give thermal properties such as melting and glass transition temperatures [56].

3.2.2 Fourier Transform Infrared Spectroscopy (FTIR)

To validate and identify the non-electroactive (α) and electroactive (β) phases of PVDF systems, Fourier transform infrared spectroscopy (FTIR) was applied. The essential components of the FTIR are exhibited in Fig. 25.

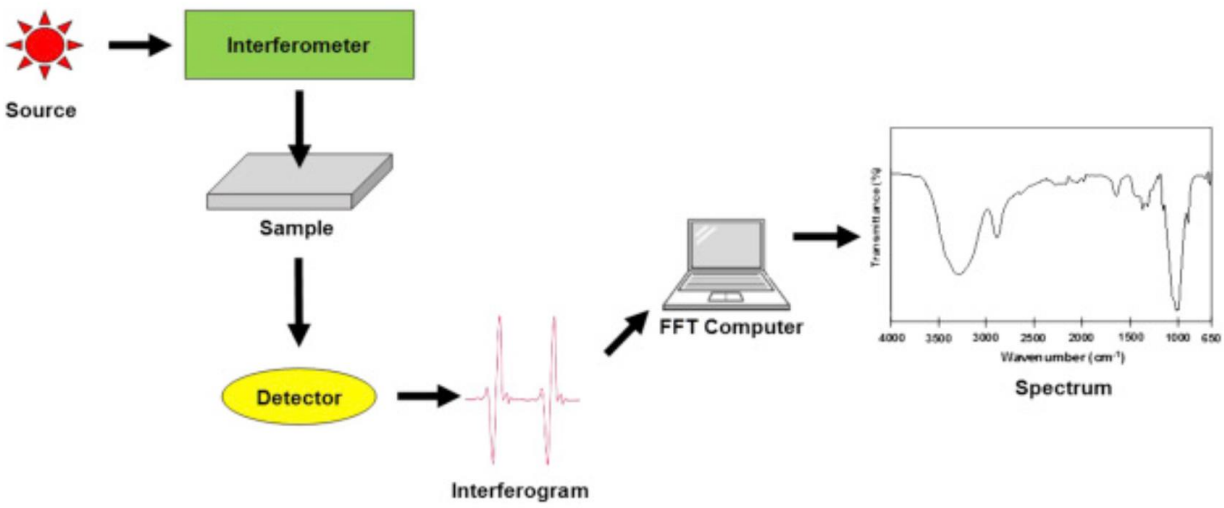

Fig. 25. Essential components of FTIR [57].

The FTIR procedure originates with an infrared light source. The light source is transmitted into an interferometer, a device that measures the wave characteristics. The beam is transmitted into the sample, where a detector senses the difference between the reference and the sample. That retardation is measured as an interferogram, where a computer uses a Fourier transform analysis to portray the spectrum of the polymer sample. In polymers, FTIR can be used to check the vibrational bands of the ligands [57].

3.3 Luminescence Techniques

The luminescence techniques performed were the use of photoluminescence equipment and the diamond anvil cell equipment. The mention of such equipment is found in sections **2.2.2 Photoluminescence** and **2.2.3 Photo-Mechanoluminescence**.

CHAPTER IV

EXPERIMENTAL PROCEDURES

The sections to be discussed in this chapter are the materials employed to create photo-mechanoluminescent systems, the preparation procedure to process them into nanofibers, and the experimental methods used to characterize such fibers.

4.1 Materials Used

The work materials were as follow:

- Polyvinylidene di-fluoride (Arkema-Kynar, PVDF, 741).
- Europium (III) Nitrate Hexahydrate ($Eu(NO_3)_3 \cdot 6H_2O$).
- Europium (III) Sulfate ($Eu_2(SO_4)_3$).
- Cerium(III) Nitrate Hexahydrate ($Eu(NO_3)_3 \cdot 6H_2O$).
- Ammonium Cerium (IV) Sulfate Dihydrate ($Ce(NH_4)_4(SO_4)_4 \cdot 2H_2O$).
- Acetone (C_3H_6O, ≥99.5%).
- N,N-Dimethylacetamide ($CH_3CON(CH_3)_2$, ≥99%).

4.2 Sample Preparation

The polymer-lanthanide solutions were prepared using different weight percentages of the lanthanide structures on a 1:1 mixture of acetone and DMA. Table 2 portrays the different dopant concentrations.

Tested Lanthanide Concentrations			
Lanthanide concentration (g)	PVDF concentration (g)	DMA (g)	Acetone (g)
0	1.1	1.95	1.95
0.1	1.1	1.95	1.95
0.25	1.1	1.95	1.95
0.5	1.1	1.95	1.95
0.75	1.1	1.95	1.95
1	1.1	1.95	1.95

Table 2. Tested Lanthanide Concentration

Table 2 portrays the different lanthanide concentrations tested for nanofiber production. The different concentrations were homogenized using a magnetic stirrer and a magnetic hot plate. The solutions were stirred at 720 RPMs for 1 hour and were mixed thoroughly as seen in Fig. 26.

Fig. 26. Representation of a PVDF-lanthanide solution.

Fig. 26 portrays a 5% weight of cerium nitrate mixed with PVDF. The variation of weight percentages of the lanthanides was implemented to find the optimum yield of nanofibers. Table 3 portrays the optimum yield of fibers using the different lanthanide concentrations.

	Lanthanide Concentration (%)						
RPM	0	1	2.5	5	7.5	10	
5500							
6000							
6500							
7000							
7500							Legend
8000							High Nanofiber Production
8500							Low Nanofiber Production
9000							No Nanofiber Production

Table 3. Optimum PVDF-Lanthanide Nanofiber Production Rate.

Table 3 represents that the optimum nanofiber production yield of the PVDF-lanthanide systems was at 5% lanthanide concentration.

4.3 Experimental Procedure for Nanofiber Production

The solution making process had a 30-min standard time to mix the powders and solvents, and it homogenized entirely for 1 hour on the oil bath. The solution was spun using the Forcespinning® Technology Cyclone 1000, depicted in Fig. 27.

Fig. 27. Forcespinning® Technology Cyclone 1000 [58].

The PVDF-lanthanide solutions were spun at 7500 RPMs for 8 minutes each cycle. Each solution lasted for two cycles. The fibers were collected using a 1” x 1” aluminum square. The use of a spinneret was required, depicted in Fig. 28.

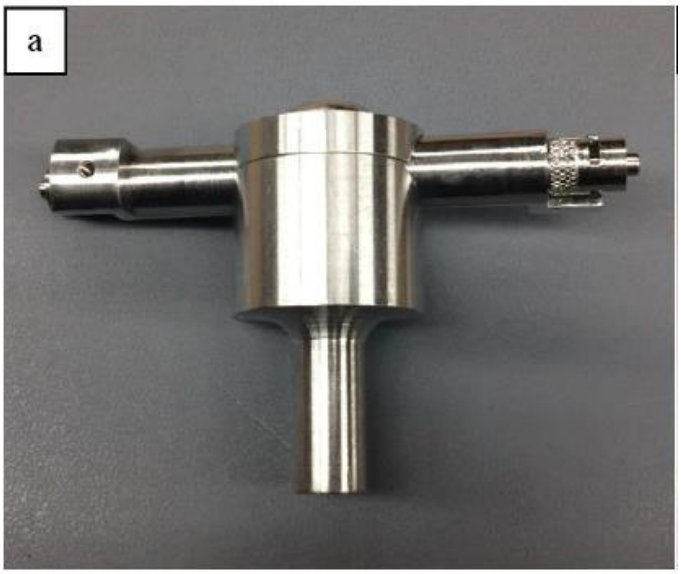

Fig. 28. Solution Spinneret [59].

1-2 mL of the polymer solution was injected into the spinneret. The spinneret rotated at high RPMs, and the centrifugal forces produced extruded the solution into a fibrillar structure.

4.4 Experimental Procedure for Mechanical Characterization Measurements

The Zeiss Sigma VP scanning electron microscope (SEM) equipment from the University of Texas Rio Grande Valley (UTRGV) was used to characterize the diameter of the polymer fibers. Fig. 29 shows the Zeiss SEM.

Fig. 29. Zeiss Sigma VP SEM equipment [58].

When running an SEM characterization procedure, the polymeric samples were sputtered with gold for 15 minutes to provide a better image. Five images were taken of each sample at 1 kV at magnifications from 200-5000X. Three-hundred measurements of each sample were analyzed to obtain the average fiber diameter.

Fig. 30. Thermo Scientific K-Alpha XPS equipment [58].

The use of Thermo Scientific K-Alpha x-ray photoelectron spectroscopy (XPS) equipment was applied to verify the composition of the fibers. The fibers were split into small

strands. The samples and the raw powder materials were secured into the XPS testing surface via the use carbon tape. The testing surface was inserted and pressurized into the vacuum chamber of the XPS. The XPS software, *Avantage*, was employed to measure three distinct surface points of each specimen. A survey and the required chemical elements of each sample were analyzed at 10 scans and at surface scan spot of 300 microns at a time. The outer layer was scanned and etched at a rate of 0.07 nm per scan.

4.5 Experimental Procedure for Phase Identification Measurements

Dynamic scanning calorimetry (DSC) and Fourier transform infrared spectroscopy (FTIR) was performed to identify the α and β polymer phases of the fiber samples. The DSC utilized was the TA DSC Q-100, as portrayed in Fig. 31.

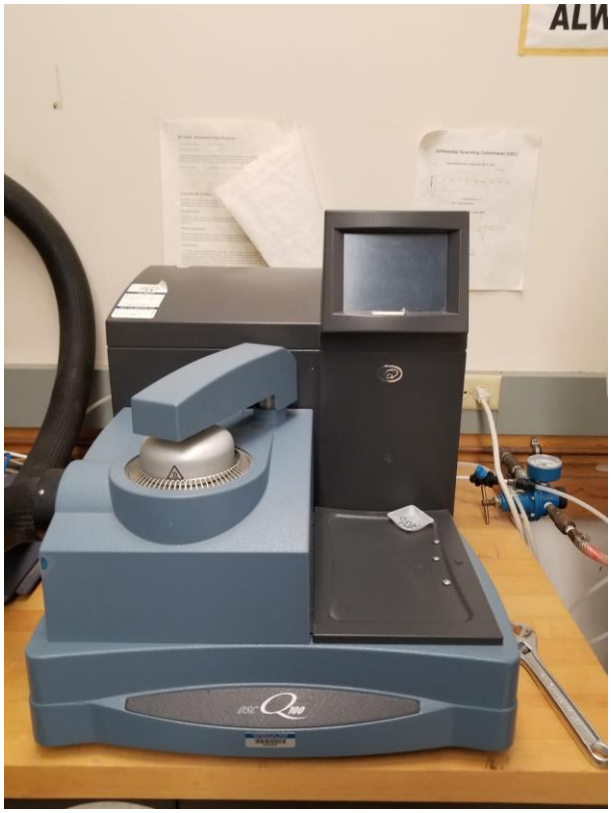

Fig. 31. TA Q-100 DSC Equipment [58].

Aluminum hermetic pans were employed to run the DSC experiment. Each fiber was measured to have a sample weight of 10 mg and then pressurized into a pan. The DSC ran a temperature heating ramp setting, as provided below:

1. Machine equilibrated at 30 °C.
2. Heated at 10 °C/min until reaching 250 °C.
3. Isothermally induced for 10 min.
4. Cooled at 10 °C/min until reaching 30 °C.
5. Heated at 10 °C/min until reaching 250 °C.
6. Isothermally induced for 10 min.
7. Cooled at 10 °C/min until reaching 30 °C .
8. Equipment state off.

Steps 2-4 symbolized the 1^{st} heating ramp or the processing ramp, and steps 5-7 represented the 2^{nd} heating ramp of the material ramp. A nitrogen generator was used at 40 ml/min to control the cooling settings of the DSC.

The FTIR used on this project was the Bruker Vertex 70 series located in the Chemistry Department at UTRGV, portrayed in Fig. 32. A background test was first performed to ensure the distinction between the reference and the test samples. The samples were preloaded one at a time, and each absorbance test ran from 4000 to 400 cm^{-1}.

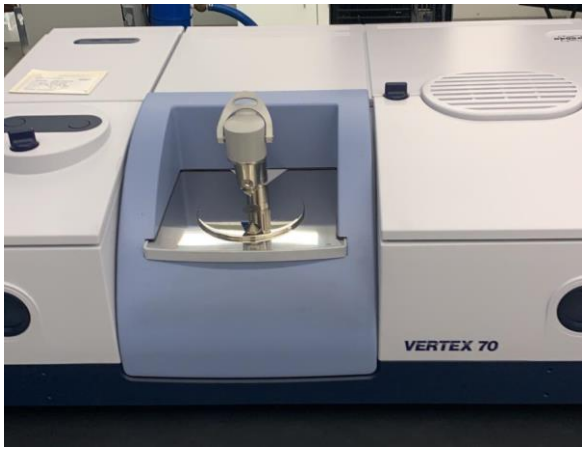

Fig. 32. Bruker Vertex 70 FTIR Equipment.

4.6 Experimental Procedure for Luminescence Measurements

To characterize the luminescence properties of the fiber samples, a photoluminescence spectrometer (PL). The use of a diamond anvil cell (DAC) was required to induce the pressurized force on the samples.

The photoluminescence equipment used was the Edinburgh Instruments FLS980 Fluorescence Spectrometer, as seen in Fig. 33. The machine has an excitation and emission spectral range from 230 to 1000 nm and 220 to 870 nm, respectively. The photomultiplier contributes to the emission spectral range and has a response width of 600 ps.

Fig. 33. Edinburgh Instruments FLS980 Fluorescence Spectrometer (PL) Equipment.

The DAC utilized was an Almax Easylab DAC equipment, portrayed in Fig. 34.

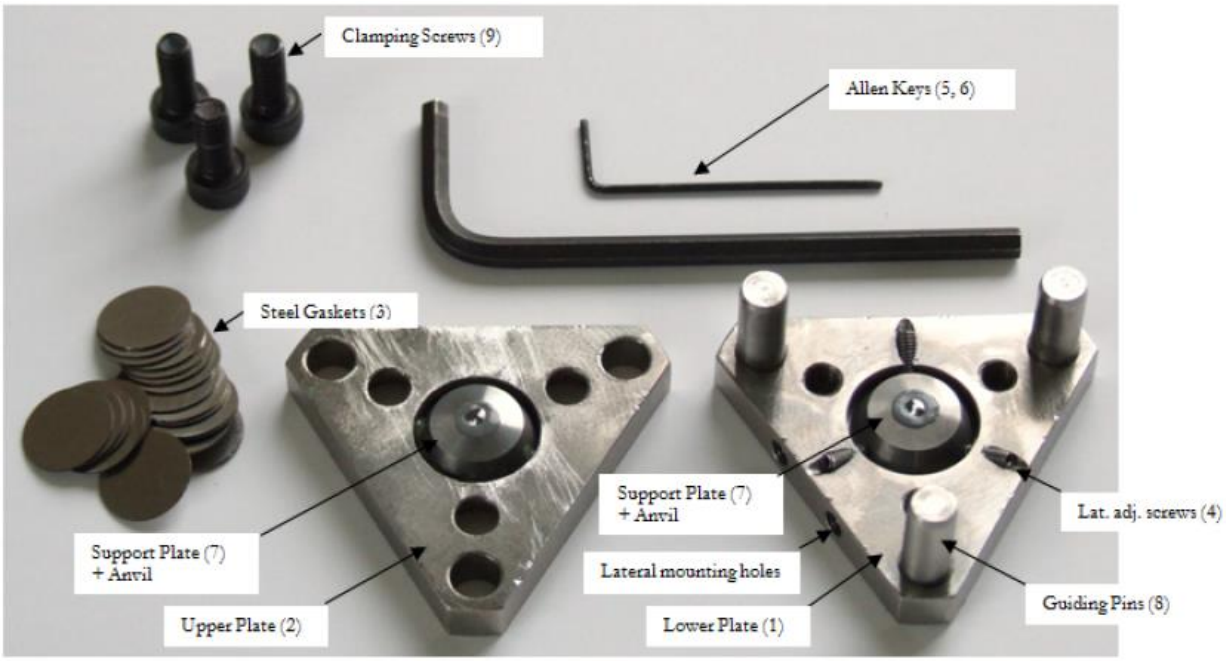

Fig. 34. Almax Easylab Diamond Anvil Cell (DAC) equipment.

The DAC upper plate contained the guiding holes to align the DAC. The bottom DAC plate contained the guiding pins, the lateral mounting holes, the adjacent lateral screws. The diamonds in the center of each plate are the ones providing the pressure in the sample. The steel gaskets served as a medium to place the fiber samples, the clamping screws to induce the pressure on the diamonds, and the Allen keys to properly enclose the upper and lower parts.

To properly test the DAC with the PL equipment, a 3d printed polylactic acid (PLA) stand was manufactured, as seen in Fig. 35.

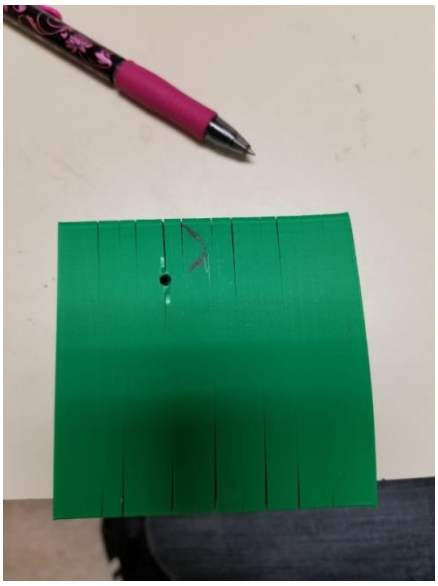

Fig. 35. PLA 3D Printed Stand.

The implementation of both, the DAC and the PL is portrayed in Fig. 36.

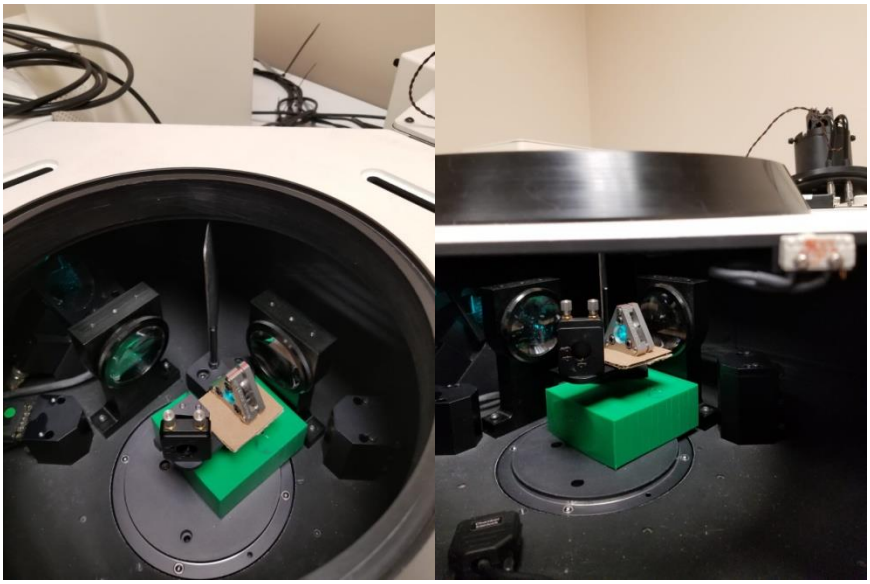

Fig. 36. DAC alignment on PL equipment.

The fiber samples were doped with ruby. The ruby does not interact with the luminescence of the fibers but used a pressure reference. This procedure is portrayed in Fig. 37.

Fig. 37. Sample and DAC alignment.

Fig. 37(a) portrays the fiber sample being doped with ruby and aligned using a microscope. Fig. 37(b) shows the DAC without the test gasket. Fig. 37(c) represents the sample gasket being loaded and aligned on the DAC.

The experimental luminescence procedure was performed as follow for each sample:

1. The fiber sample was doped with ruby and loaded between the steel gaskets.
2. The sample gasket was aligned on the DAC using a microscope.
3. The upper part of the DAC was assembled.
4. Using the 3d printed stand, the DAC was aligned with the PL system.
5. An excitation survey was performed on the PL system.
6. With the excitation known, the PL system ran at that wavelength.
7. The emission wavelengths were recorded.
8. The DAC was removed from the PL system, and clamping screws were twisted ¼ of a turn via the use of the Allen wrenches.
9. The DAC was aligned on the PL system, ran at the known excitation wavelength, and the emission wavelength was recorded.
10. Steps 8 and 9 were performed seven times.
11. The pressure was removed from the DAC system, the PL ran the known excitation wavelength, and the emission wavelength was recorded.

CHAPTER V

RESULTS AND DISCUSSIONS

The following paragraphs are the results gathered from the creation of photo-mechanoluminescent polymer fibers. SEM was used to evaluate the fiber diameter, XPS to verify the composition of the fibers, DSC to evaluate crystalline composition, FTIR to quantify the β phase, and the pressure-induced luminescence equipment to analyze the luminescence of the samples under pressure. The nomenclature for the samples are as following:

- PVDF Control = PVDF fibers, no lanthanides added.
- PVDF Eu Ni = PVDF fibers doped with europium nitrate 5% weight.
- PVDF Eu Su = PVDF fibers doped with europium sulfate 5% weight.
- PVDF Ce Ni = PVDF fibers doped with cerium nitrate 5% weight.
- PVDF Ce Su = PVDF fibers doped with cerium sulfate 5% weight.

5.1 Scanning Electron Microscope (SEM) Data

Figures 38-42 are high resolution SEM photos of the developed samples, alongside a gaussian-belt distribution of the fiber diameters.

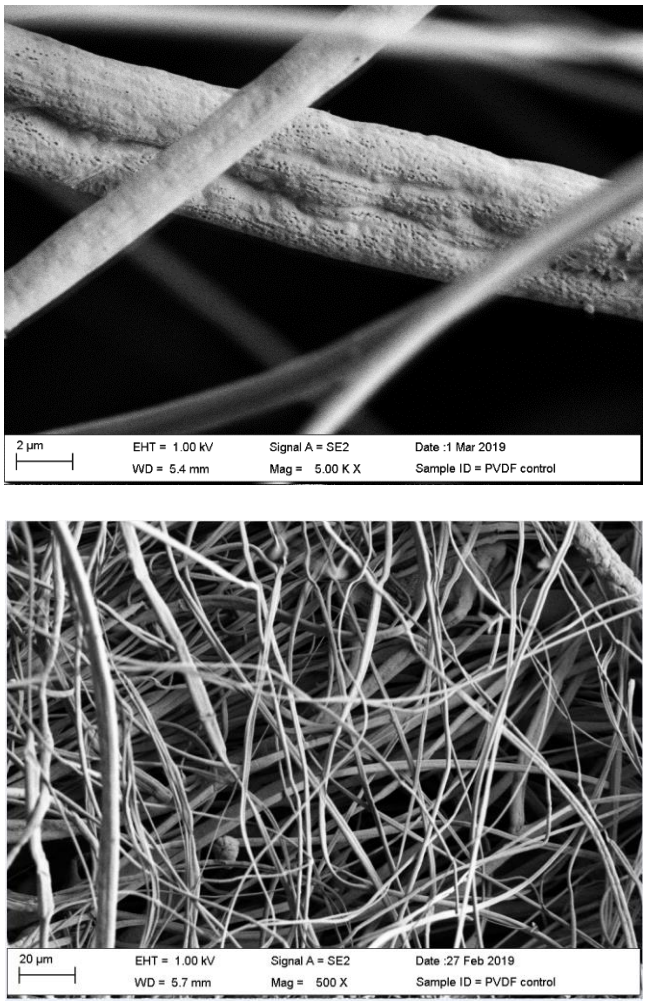

Fig. 38. SEM images and nanofiber distribution from PVDF Control.

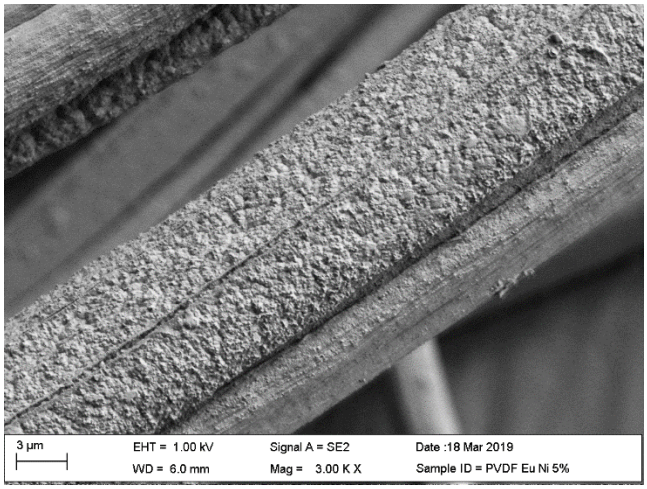

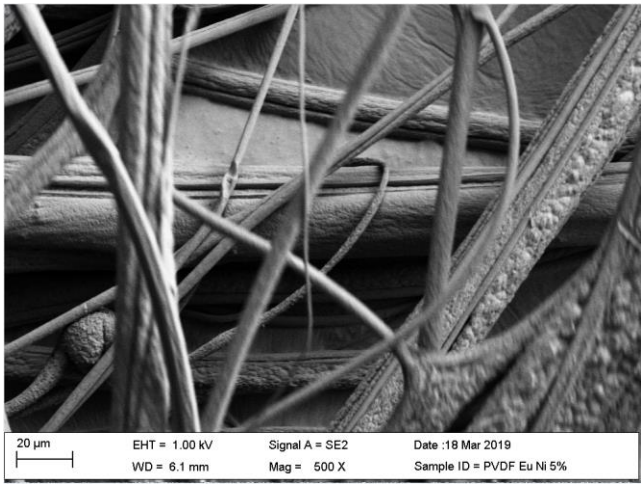

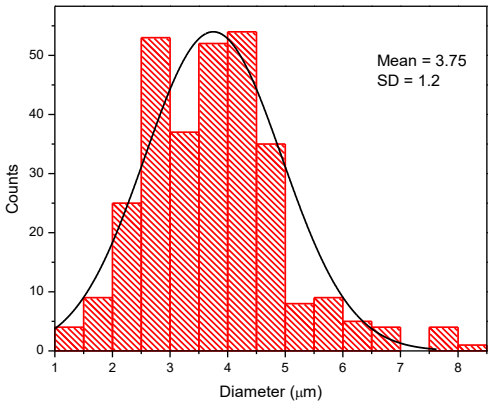

Fig. 39. SEM images and nanofiber distribution from PVDF Eu Ni.

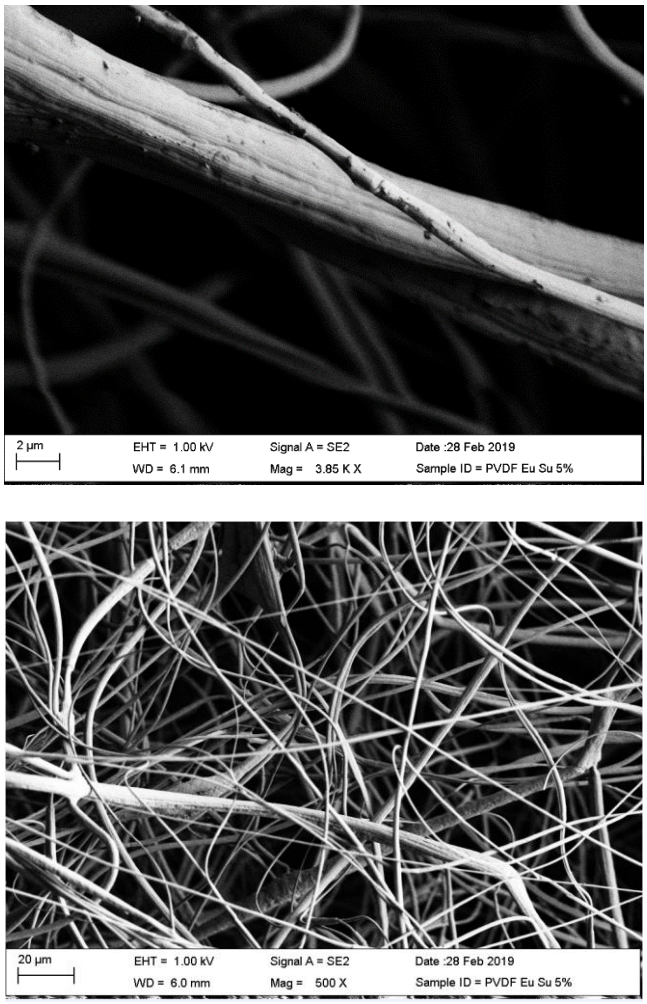

Fig. 40. SEM images and nanofiber distribution from PVDF Eu Su.

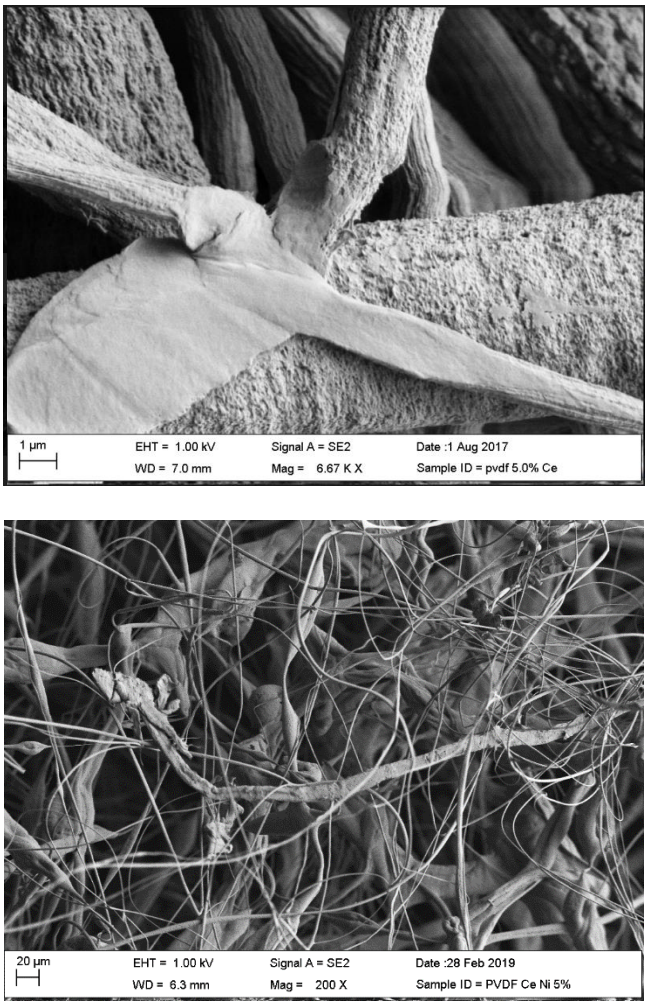

Fig. 41. SEM images and nanofiber distribution from PVDF Ce Ni.

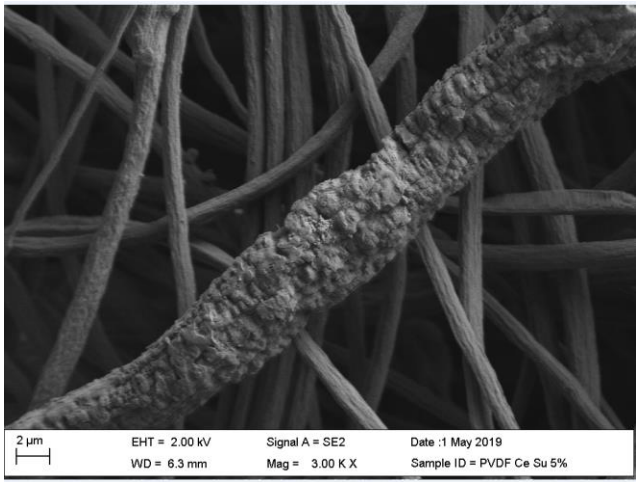

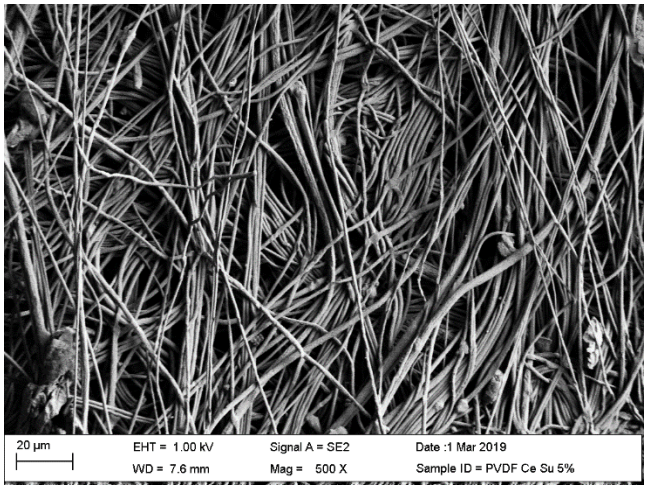

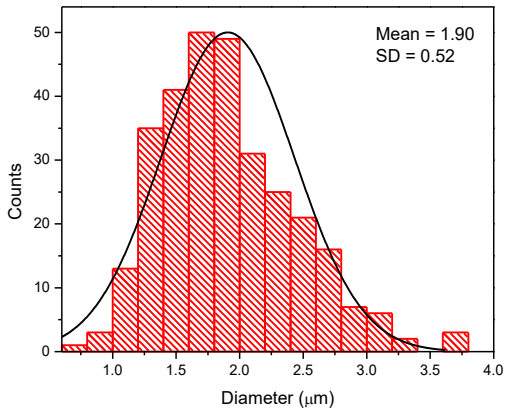

Fig. 42. SEM images and nanofiber distribution from PVDF Ce Su.

The PVDF Control and PVDF Ce Su have a smooth fiber surface compared to the other samples. PVDF Eu Ni and PVDF Ce Ni have rough surfaces, while the first has a homogenous surface. Also, the SEM images portrayed the finding of conjoined fibers and unidirectional fibers, as portrayed in Fig. 38 and 42. Table 4 portrays the fiber diameter of the polymer-lanthanide systems, and their standard deviation. It was found that the samples were in the micron range.

Sample	Diameter (microns)	Standard Deviation
PVDF Control	2.87	0.8
PVDF Eu Ni	3.75	1.2
PVDF Eu Su	2.56	0.74
PVDF Ce Ni	3.07	0.9
PVDF Ce Su	1.9	0.52

Table 4. Fiber Diameter and Standard Deviation of Polymer-Lanthanide Systems.

5.2 X-Ray Photoelectron Spectroscopy (XPS) Data

Figures 43 to 53 are the XPS data from the lanthanide powders and the PVDF-lanthanide fiber systems.

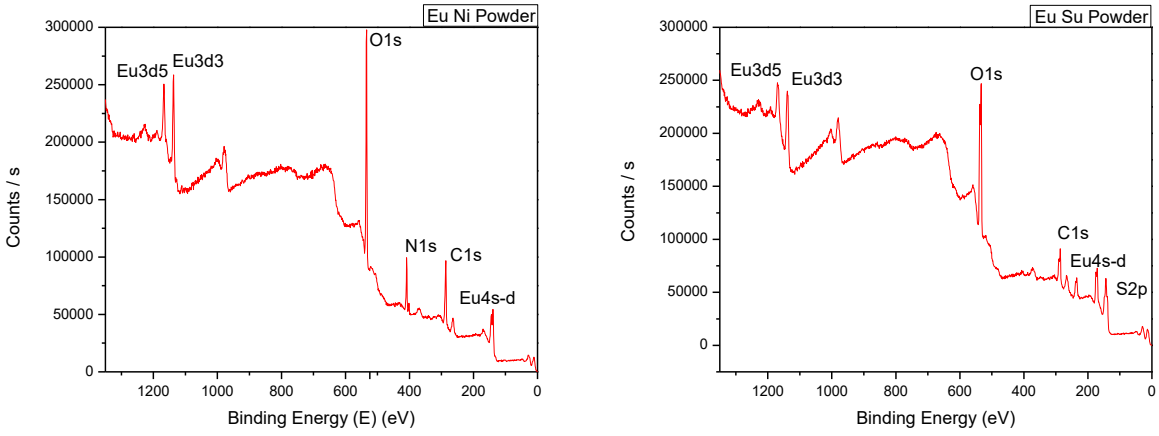

Fig. 43. XPS Survey of Europium Nitrate (a) and Sulfate (b) Powders.

Fig. 43 portrays the XPS survey spectrum of the europium lanthanides powders. The survey found europium, oxygen, and carbon on both samples. The survey spectrum detected nitrogen and sulfur for the nitrate and sulfate powders, respectively.

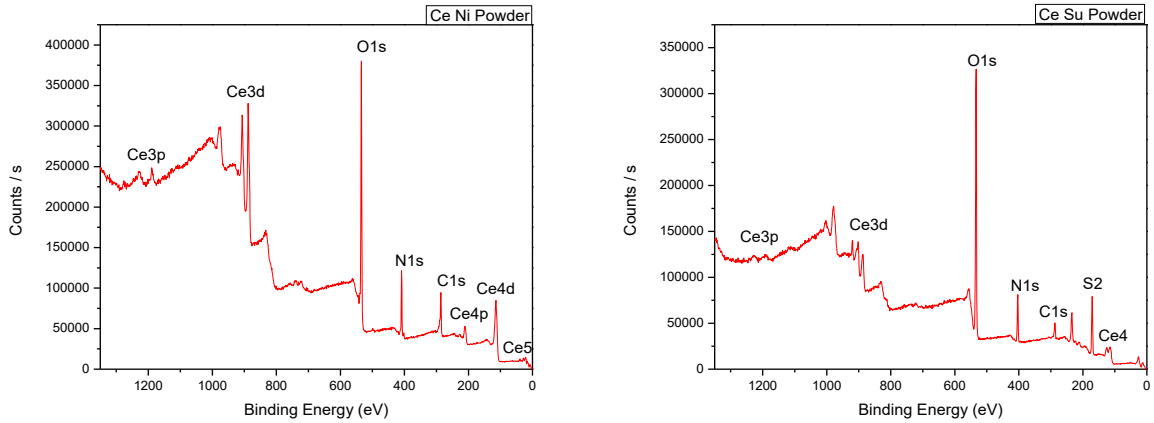

Fig. 44. XPS survey of Cerium Nitrate (a) and Sulfate (b) Powders.

Fig. 44 presents the lanthanide cerium powders. The XPS survey spectrum analyzed the powders and found cerium, oxygen, nitrogen, and carbon on both samples. The sulfate sample contains sulfur and nitrogen because of its chemical structure.

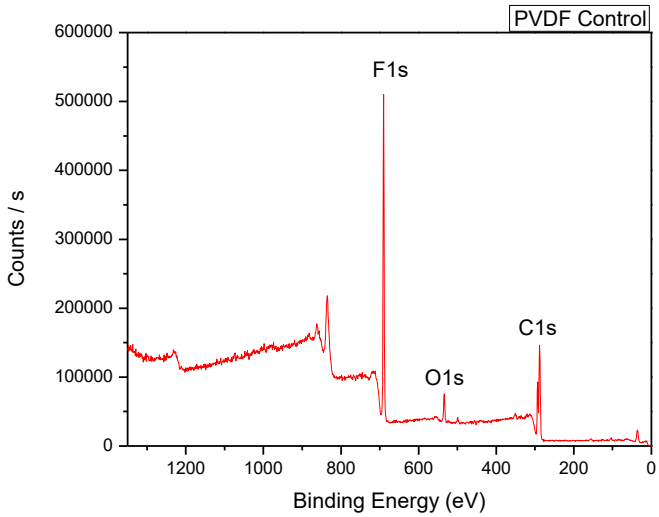

Fig. 45. XPS survey of PVDF Control Fibers.

Fig. 45 portrays XPS survey for PVDF control fibers. The polymer chemical structure contains fluorine, oxygen, and carbon, as expected in the XPS survey.

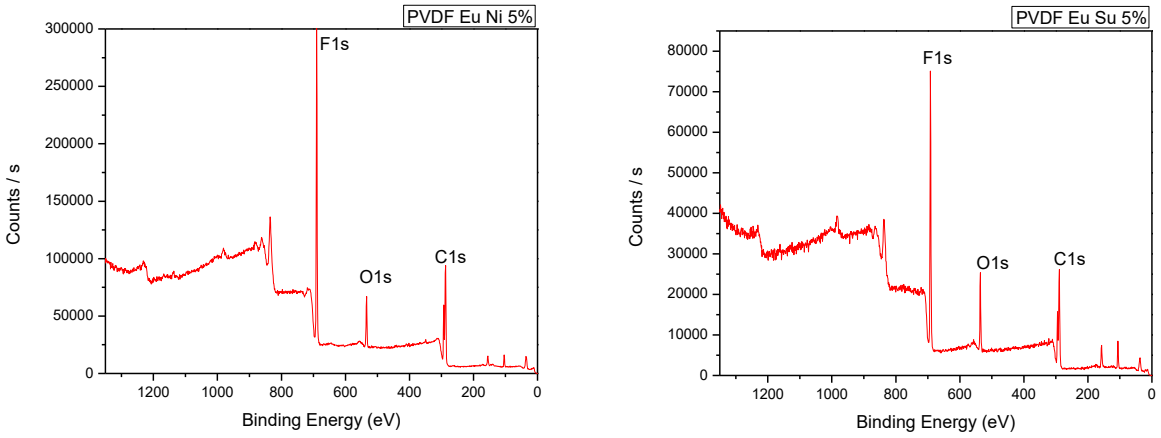

Fig. 46. XPS survey of PVDF Eu Ni (a) and PVDF Eu Su (b) Fibers.

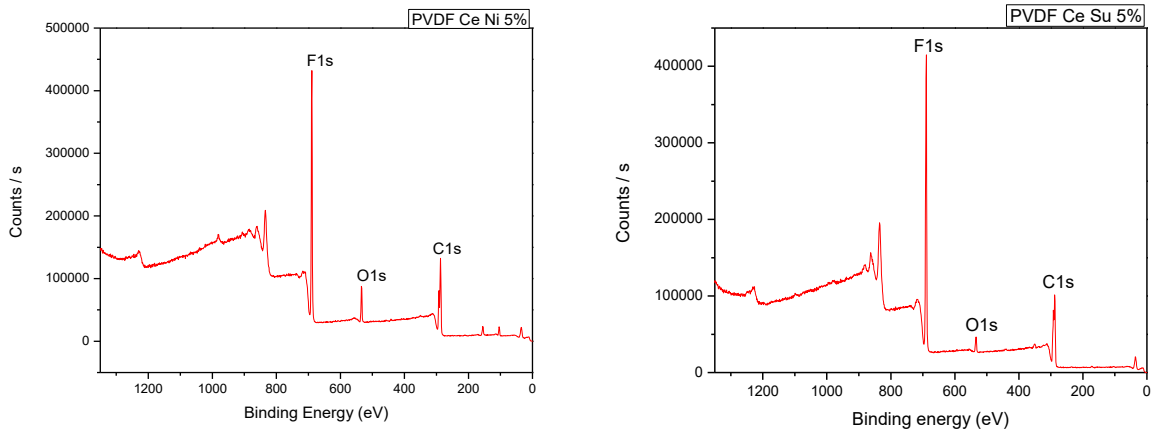

Fig. 47. XPS survey of PVDF Ce Ni (a) and PVDF Ce Su (b) Fibers.

Figures 46 and 47 show the PVDF-lanthanide fibers the XPS survey detected fluorine, oxygen, and carbon. The XPS survey does not detect the europium and cerium elements due to the polymer concentration being higher than the lanthanides.

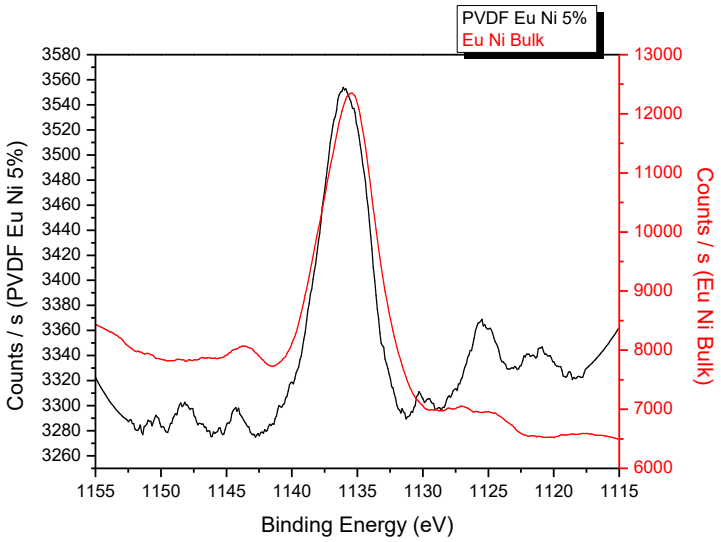

Fig. 48. XPS Europium Spectrum of Eu Ni Powder (red) and PVDF Eu Ni Fibers (black).

Fig. 48 compares the PVDF Eu Ni fibers europium spectrum to the europium nitrate powder. The distinctive europium peak is presented in both samples.

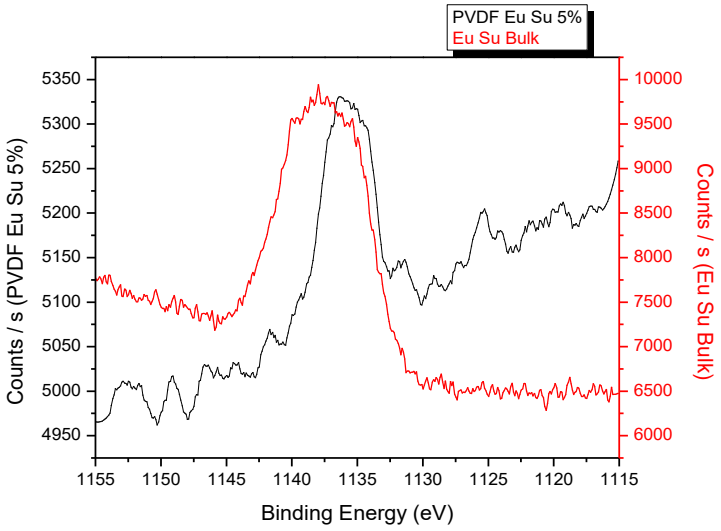

Fig. 49. XPS Europium Spectrum of Eu Su Powder (red) and PVDF Eu Su Fibers (black).

An XPS europium spectrum of the PVDF Eu Su fibers was compared to the europium sulfate powder. The PVDF Eu Su europium peak is shifted to the right in comparison to the europium sulfate powder; nonetheless, the distinctive europium peak is found in both samples.

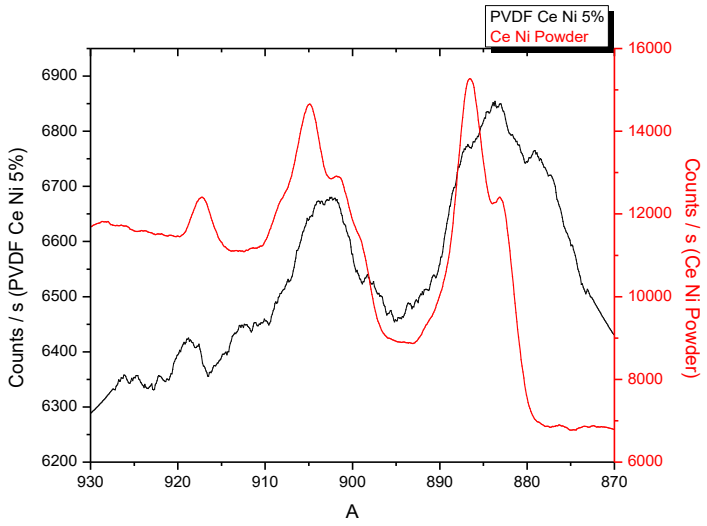

Fig. 50. XPS Cerium Spectrum of Ce Ni Powder (red) and PVDF Ce Ni Fibers (black).

Fig. 50 present the XPS cerium spectrum of the PVDF Ce Ni fibers compared to the cerium nitrate powder. The distinctive cerium peaks are found in both samples, with the PVDF Ce Ni peaks shifted to the right.

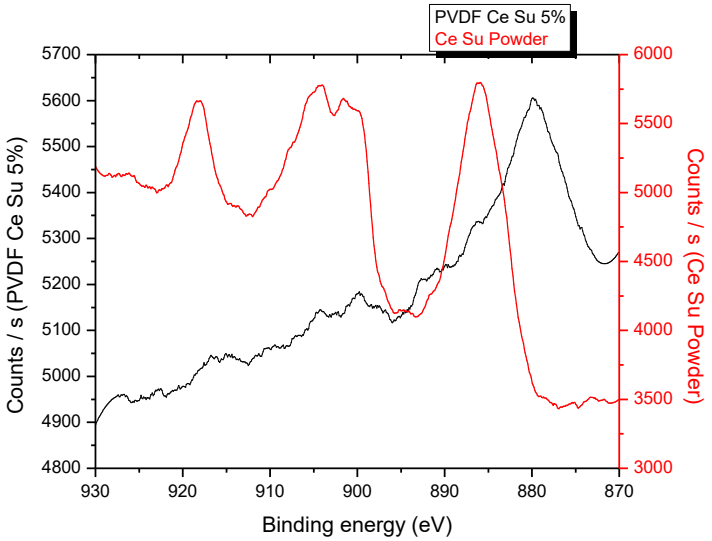

Fig. 51. XPS Cerium Spectrum of Ce Su Powder and PVDF Ce Su Fibers.

An XPS cerium spectrum of the PVDF Ce Su fibers was compared to the cerium sulfate powder, as seen in Fig. 51. The distinctive luminescence cerium peak is found in the 880 to 890 range; both samples contain the distinctive peak.

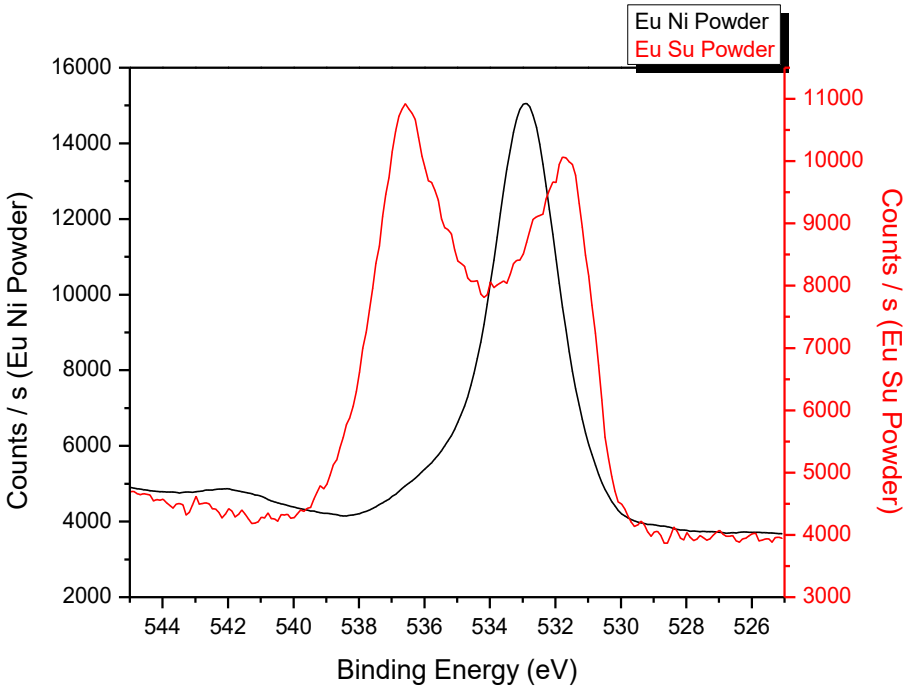

Fig. 52. XPS Oxygen Spectrum of Europium Nitrate (black) and Sulfate (red) Powders.

The XPS machine analyzed the oxygen spectrum on the europium powders. The powders chemical structure portrays the lanthanides distinctive oxygen peaks; for instance, europium nitrate powder has a distinctive oxygen peak, while the europium sulfate has two. The oxygen impacts the color of the europium, one peak gives a distinctive red luminescence, while two oxygen peaks have an orange luminescence [60].

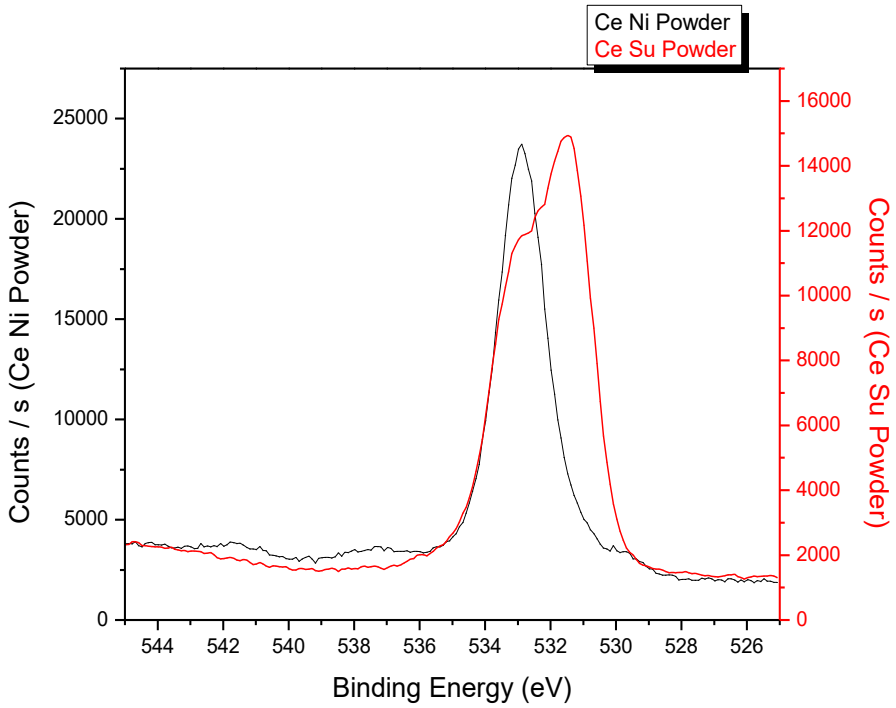

Fig. 53. XPS Oxygen Spectrum of Cerium Nitrate (black) and Sulfate (red) Powders.

The XPS equipment analyzed the oxygen spectrum of the cerium powders. The distinctive oxygen peaks symbolize the blue-violet cerium luminescence.

The XPS data confirmed the composition of the polymer-lanthanide samples. The lanthanide powders and the polymer fibers chemical structure was verified using the XPS equipment. The polymer-lanthanide systems contained the expected elements.

5.3 Differential Scanning Calorimetry (DSC) Data

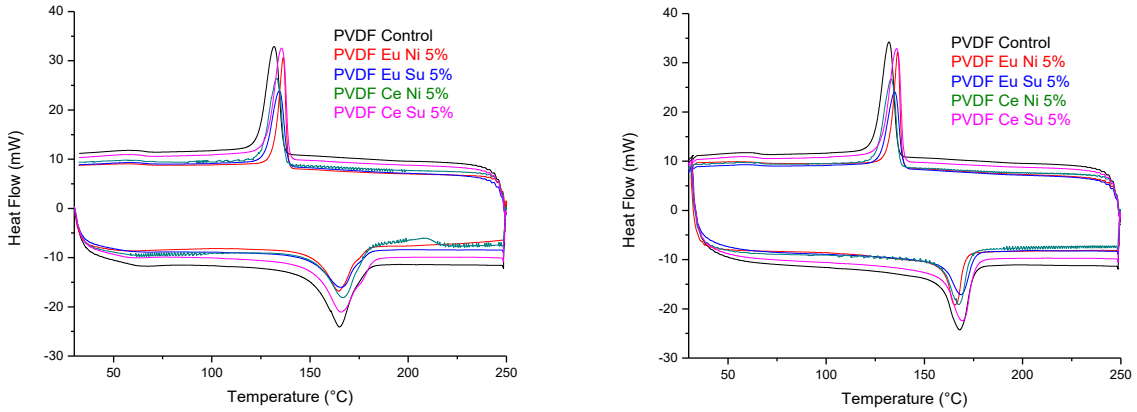

Fig. 54. DSC Data for Polymer-Lanthanide Samples (a) First and (b) Second Run.

Fig. 54 portrays the processability (a), and the material (b) runs, where the data portrays the exothermic and endothermic peaks, and the melting and crystallization temperatures can be analyzed.

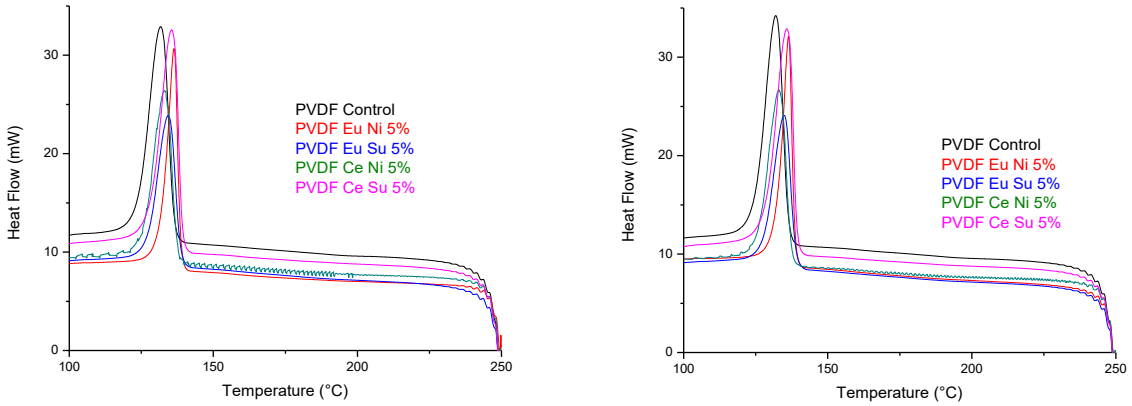

Fig. 55. Scaled-up Version of DSC Exothermic Peaks (a) First and (b) Second Run.

Fig. 55 presents a scaled-up version of the exothermic peaks. The left side portrays the processability (a) 1st run and the right the material (b) 2nd run.

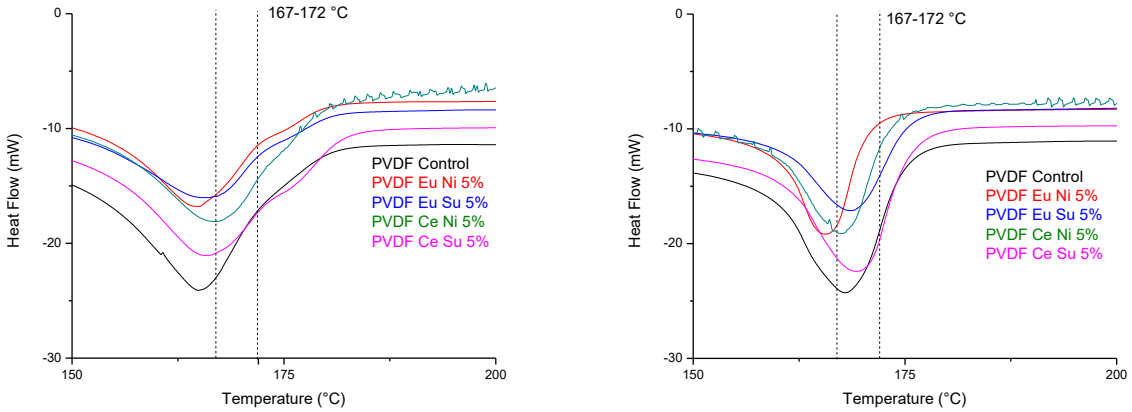

Fig. 56. Scaled-up Version of DSC Endothermic Peaks (a) First and (b) Second Run.

Fig. 56 portrays the scaled-up version of the endothermic peaks. The 167-172 °C temperature range indicates the location of the α and β phases. The endothermic peak closer to 167 °C represents the α peak, the second distinctive peak symbolizes the β phase. In the processability run, it seen two peaks, the α and β peaks. The material run depicts only one peak, the α peak.

	Percentage of Crystallinity on 1st Run	Percentage of Crystallinity on 2nd Run	Percentage change of Crystallinity
PVDF Control	62.2	50.6	22.9
PVDF Eu Ni	59.2	45.8	29.2
PVDF Eu Su	54.9	44.4	23.4
PVDF Ce Ni	61.9	40.9	51.2
PVDF Ce Su	61.3	46.7	31.3

Table. 5. Crystallinity of Polymer-Lanthanide Samples.

Table 5 depicts the crystallinity percentage of polymer-lanthanide samples. The samples exhibit a higher crystallinity percentage on the 1st run (processability) than on the 2nd run.

	Melting Temperature (°C) on 1st Run	Melting Temperature (°C) on 2nd Run	Temperature change
PVDF Control	164.9	168	3.1
PVDF Eu Ni	164.9	165.7	0.8
PVDF Eu Su	166.2	168.9	2.7
PVDF Ce Ni	167.4	167.7	0.3
PVDF Ce Su	165.9	169.6	3.7

Table 6. Melting Temperature peaks of Polymer-Lanthanide Samples.

Table 6 represents the melting temperature peaks of the polymer-lanthanide samples. The table depicts a change in the melting temperatures; the peaks are shifted to higher temperatures on the 2nd run.

The DSC data shows the crystallinity composition of the PVDF-lanthanide samples. The endothermic peaks in the 1st run (processability) portray the α and β phases, while the 2nd run (material) portrays only the α phase. The processability run has a higher crystallinity degree than the material path. The melting temperature exhibits a right peak shift from the 1st run to the 2nd run. Even though the β is analyzed on the DSC, the testing required to quantify the β phase is via the utilization of the FTIR equipment.

5.4 Fourier Transform Infrared Spectroscopy (FTIR) Data

PVDF-lanthanide fibers DSC data are shown in Figures 54 to 56.

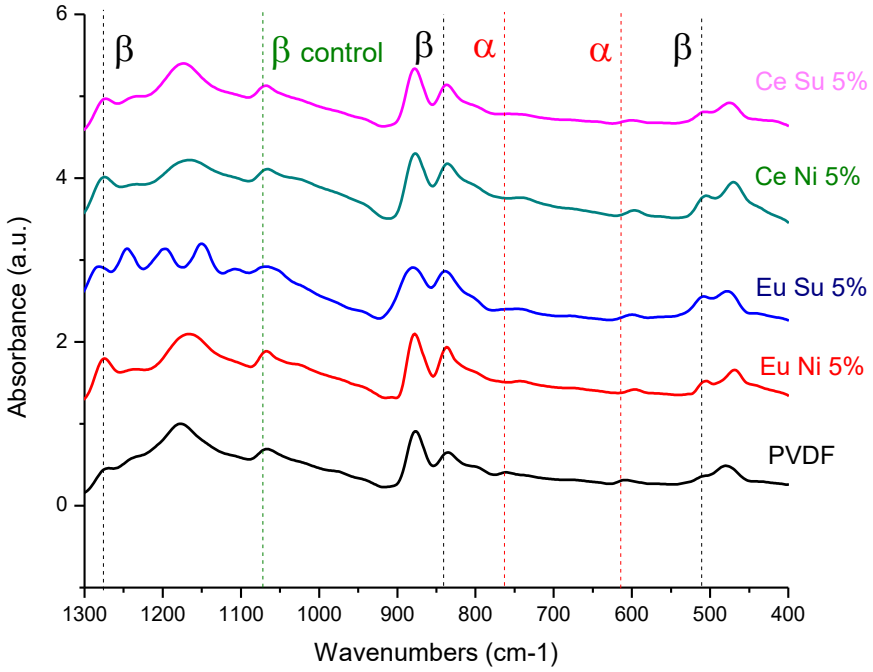

Fig. 57. FTIR Data from 1300 cm^{-1} to 400 cm^{-1}.

Fig. 57 represents the FTIR data from 1300 cm^{-1} to 400 cm^{-1} of the PVDF-lanthanide samples. The bands at 1276, 840, 510 cm^{-1} portray the β phase peaks of the polymer, while the bands at 763 and 614 cm^{-1} the represent the α phase. The β-control peak is depicted at the 1072 cm^{-1} and is constant regardless of the crystalline alterations, such as doping lanthanide agents.

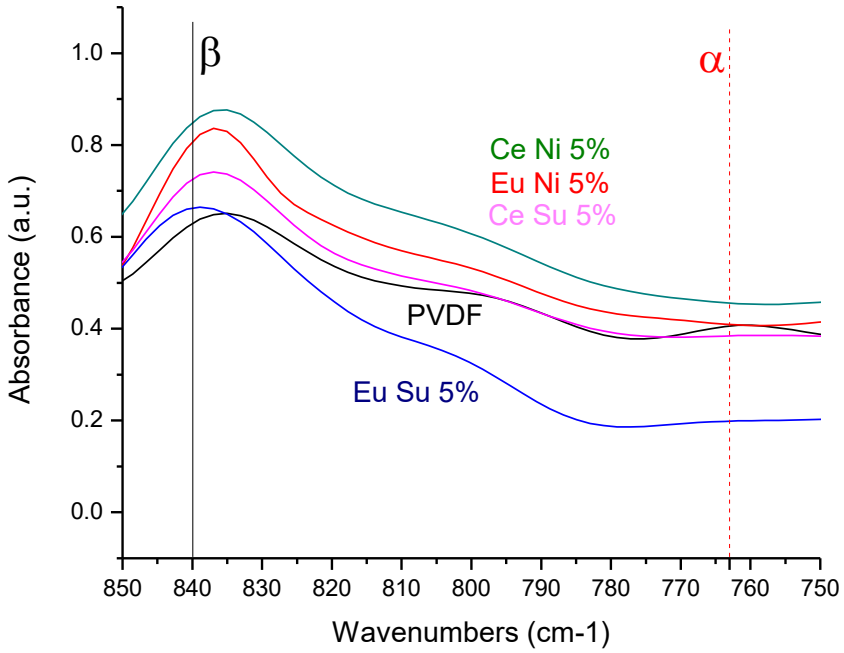

Fig. 58. Scaled-up FTIR Data from 850 cm^{-1} to 750 cm^{-1}.

Fig. 58 portrays the scaled-up version of the FTIR data of the polymer-lanthanide systems. The β phase is depicted in the 840 cm^{-1} band, and the α phase at the 763 cm^{-1} band. There is a peak at the 763 cm^{-1} band on the PVDF Control; however, on the lanthanide samples, the α phase is smoothed.

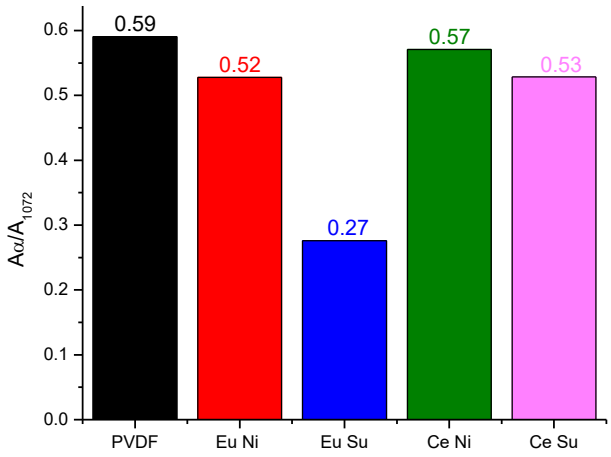

Fig. 59. Absorbance Ratio of Alpha Phase.

Fig. 59 presents the absorbance ratio of the α phase at the 763 cm^{-1} band to the β-control peak, depicted at the 1072 cm^{-1}. As the doping agents are added, the α phase ratio decreases.

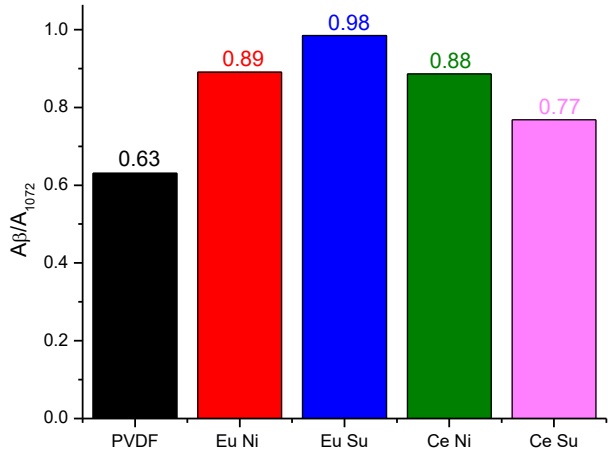

Fig. 60. Absorbance Ratio of Beta Phase.

Fig. 60 presents the absorbance ratio of the β phase at the 840 cm^{-1} band to the β-control peak, depicted at the 1072 cm^{-1}. As the doping agents are added, the β phase ratio increases.

$$F(\beta) = \frac{A_\beta}{\left(\frac{K_\beta}{K\alpha}\right)A_\alpha + A_\beta} * 100$$

Fig. 61. Lambert-Beer Law.

To quantify the relative beta phase fraction of the polymer-lanthanide samples, the lambert-beer law was utilized. The A_α and A_β are the absorbances at peaks 764 and 840 cm^{-1}, respectively. K_α (6.1 x 104 cm^2 mol^{-1}) and K_β (7.7 x 104 cm^2 mol^{-1}) are the absorption coefficients.

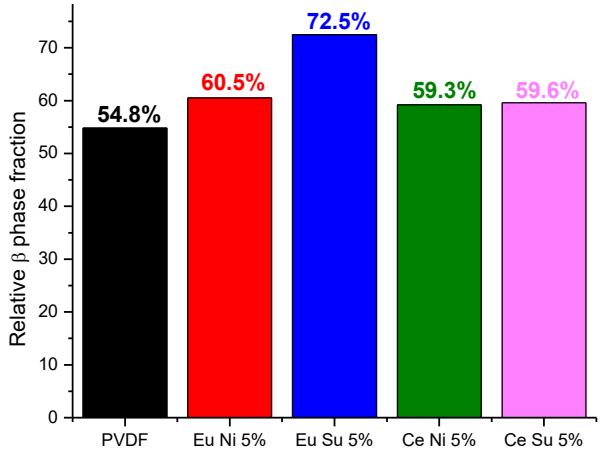

Fig. 62. Relative Beta Phase Fraction.

The relative β phase fraction is measured using the Lambert-Beer law. The β phase increases as the lanthanides are added.

FTIR data has been utilized to validate and identify the phases of PVDF-lanthanide systems because the non-electroactive α phase and the electroactive β phase can be clearly quantified using such equipment. It was discovered that as the lanthanides are added, the α phase ratio is decreased, while the β phase is increased. Also, the relative β phase fraction is increased.

5.5 Pressure Induced Luminescence (PL-DAC) Data

Ruby is doped on the polymer-lanthanide samples to act as a pressure recording system. Ruby is excited at 445 nm and does not alter the excitation or emission of the polymer samples. Depending on the ruby emission changes, the pressure is recorded. Europium and cerium samples are excited at 270 and 300 nm, respectively. The emission of the polymer-lanthanide samples is recorded and graphed into a chromaticity chart on an x and y coordinate system. The table is provided alongside the chart and depicts the changes in x and y points as pressure is induced into the system. Figures 63 to 72 portray the PVDF lanthanide fibers pressure-induced data.

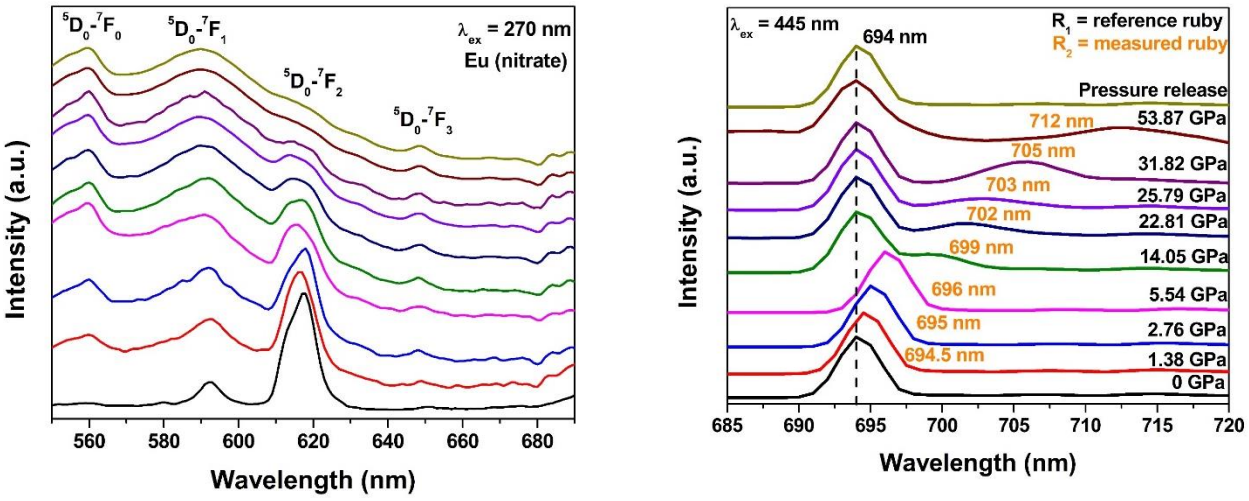

Fig. 63. Pressure Induced Data for PVDF Eu Ni.

Fig. 63 shows the pressure induced data for PVDF Eu Ni. The right graph shows the intensity change of ruby, and the pressure is recorded. The left graph portrays the PVDF Eu Ni emission graph. Before pressure is induced in the system, the PVDF Eu Ni sample exhibits a high electronic dipole transition around 620 nm. As pressure is induced, the peak at $^5D_0$-$^7F_2$ area decreases, while the magnetic dipole transition at 590 broadness.

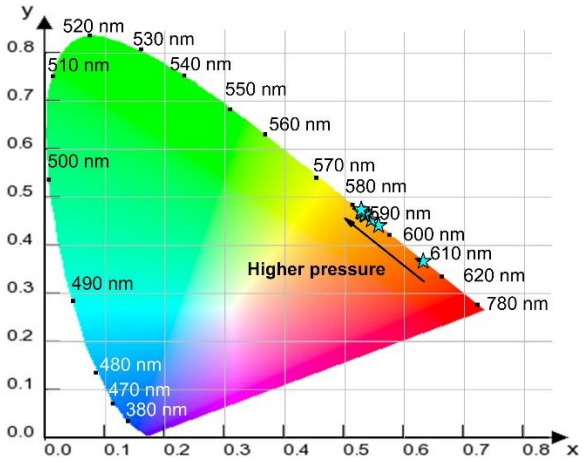

Fig. 64. Chromaticity Chart and Table for PVDF Eu Ni.

Pressure (Gpa)	x	y	n	Temperature (K)
0	0.630499	0.369005	1.631098	2007.373
1.38	0.556149	0.442822	0.87278	1978.677
2.76	0.544207	0.454675	0.789828	2126.389
5.54	0.526884	0.471852	0.681765	2371.997
14.05	0.534621	0.464189	0.728357	2258.541
22.81	0.533188	0.465613	0.719523	2279.163
25.79	0.528963	0.4698	0.69402	2341.027
31.82	0.526507	0.472245	0.679512	2377.78
53.87	0.527212	0.471541	0.683657	2367.165
Pressure released	0.527356	0.475541	0.674709	2390.198

Table 7. Luminescence Coordinates for PVDF Eu Ni.

The chromaticity chart portrays the luminescence color of PVDF Eu Ni. The table shows the x and y coordinates as pressure is induced into the system. Before being compressed, PVDF Eu Ni portrayed a red luminescence. As the pressure is induced, the system depicted a change from red to orange luminescence. The change was first recorded with a pressure of 1.4 GPa.

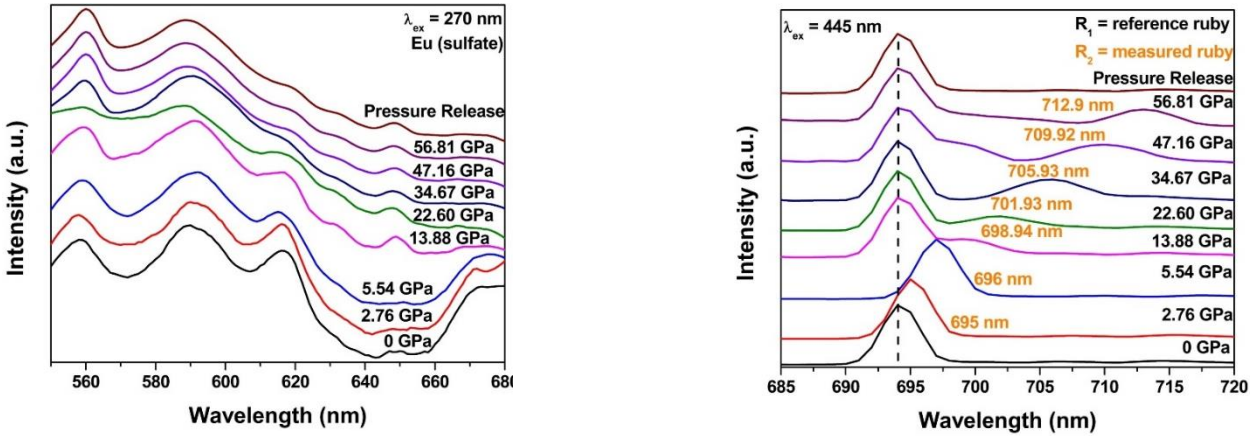

Fig. 65. Pressure Induced Data for PVDF Eu Su.

Fig. 65 shows the pressure induced data for PVDF Eu Su. The right graph shows the intensity change of ruby, and the pressure is recorded. The left graph portrays the PVDF Eu Su emission graph. Before pressure is induced in the system, the PVDF Eu Su sample exhibits three distinctive peaks; at 560, 590, and 620 nm. As pressure is induced, the peak at 620 nm decreases.

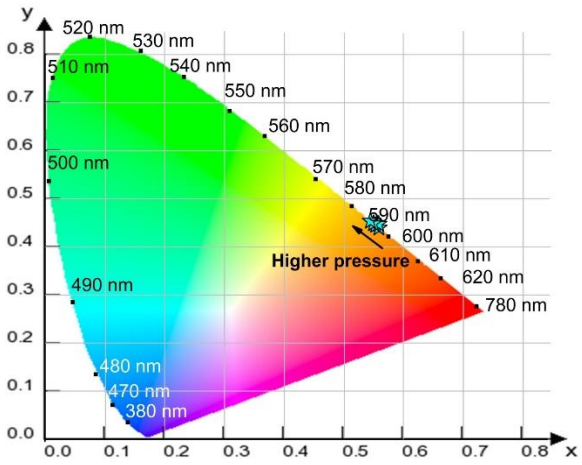

Fig. 66. Chromaticity Chart and Table for PVDF Eu Su.

Pressure (GPa)	x	y	n	Temperature (K)
0	0.558122	0.440996	0.886767	1957.14
2.76	0.557819	0.441301	0.884521	1960.54
5.54	0.552588	0.446503	0.846777	2021.27
13.88	0.550287	0.448791	0.830649	2049.38
22.60	0.549307	0.449765	0.823866	2061.59
34.67	0.549041	0.450027	0.822041	2064.92
47.16	0.544133	0.454911	0.78886	2128.32
56.81	0.543867	0.455176	0.787095	2131.85
Pressure released	0.543985	0.455295	0.787185	2131.67

Table 8: Luminescence Coordinates for PVDF Eu Su.

The chromaticity chart portrays the luminescence color of PVDF Eu Ni. The table shows the x and y coordinates as pressure is induced into the system. Before and after being compressed, PVDF Eu Su portrays an orange luminescence. As the pressure is induced, the system depicted a slight change in luminescence.

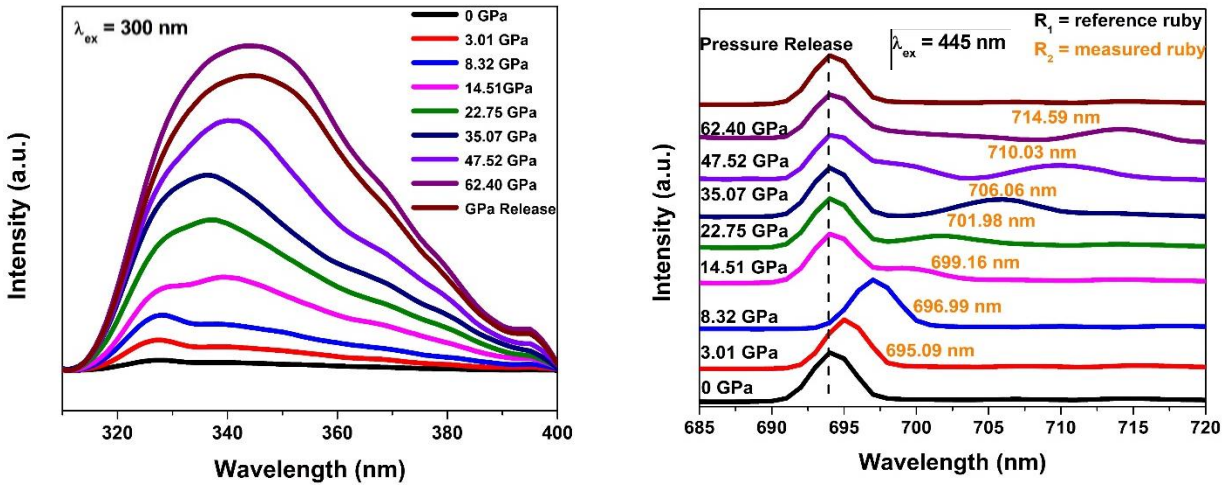

Fig. 67. Pressure Induced Data for PVDF Ce Ni.

Fig. 67 shows the pressure induced data for PVDF Ce Ni. The right graph shows the intensity change of ruby, and the pressure is recorded. The left graph portrays the PVDF Ce Ni emission graph. Before pressure is induced in the system, the PVDF Eu Su sample exhibits a slight peak at 327 nm. As pressure is induced, the peak centroid shifts to the right, until reaching 345 nm at 62.40 GPa.

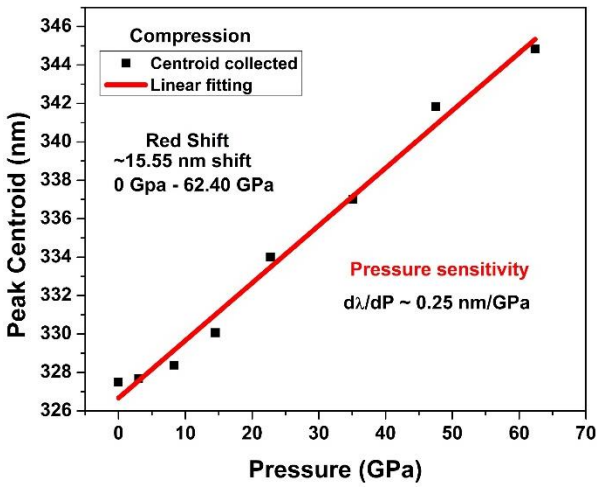

Fig. 68. Peak Centroid Change as Pressure Induced on PVDF Ce Ni.

Fig. 68 depicts the peak centroid of PVDF Ce Ni as pressure is induced. Before compression, the system centroid emits at 327 nm. As pressure is induced, the centroid shifts to

higher nm. The system experiences a 15.55 nm shift from 0 to 62 GPa. As pressure is released, the system exhibits permanent luminescence deformation, staying at 345 nm.

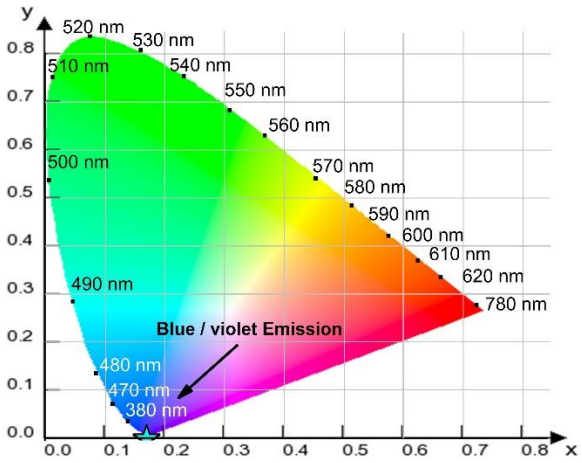

Fig. 69. Chromaticity Chart and Table for PVDF Ce Ni.

Pressure (GPa)	x	y	n	Temperature (K)
0	0.17	0.002	0.880435	1966.77
3.01	0.17	0.003	0.885246	1959.44
8.32	0.17	0.003	0.846777	1959.44
14.51	0.17	0.003	0.830649	1959.44
22.75	0.17	0.003	0.823866	1959.44
35.07	0.17	0.003	0.822041	1959.44
47.52	0.17	0.003	0.78886	1959.44
62.40	0.17	0.003	0.787095	1959.44
Pressure released	0.17	0.003	0.787185	1959.44

Table 9: Luminescence Coordinates for PVDF Ce Ni.

The chromaticity chart portrays the luminescence color of PVDF Ce Ni. The table shows the x and y coordinates as pressure is induced into the system. Before and after being compressed, PVDF Ce Ni portrays a blue-violet luminescence. As the pressure is induced, the system depicted a slight change in luminescence.

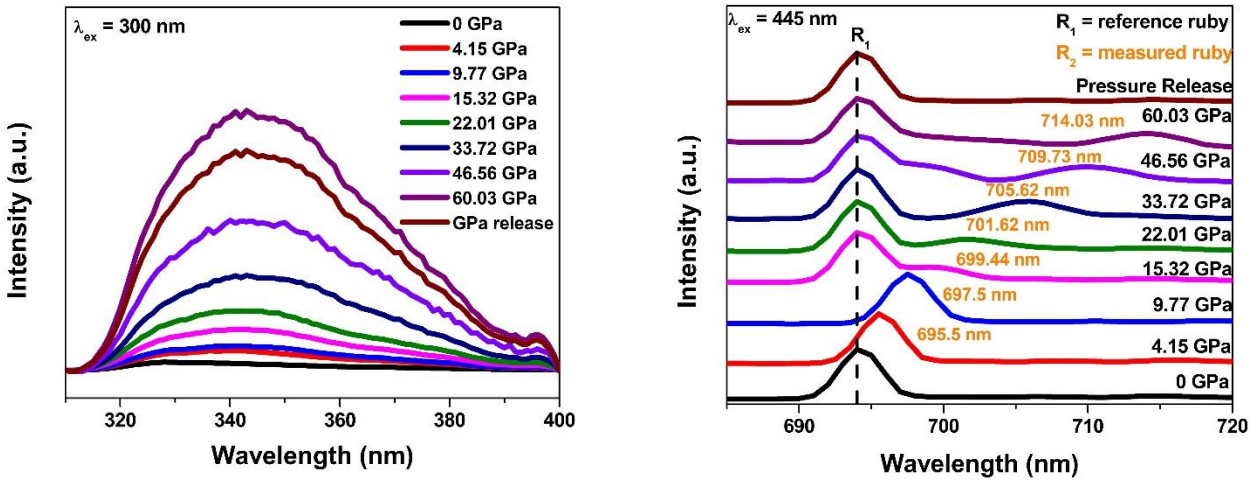

Fig. 70. Pressure Induced Data for PVDF Ce Su.

Fig. 70 shows the pressure induced data for PVDF Ce Su. The right graph shows the intensity change of ruby, and the pressure is recorded. The left graph portrays the PVDF Ce Su emission graph. Before pressure is induced in the system, the PVDF Eu Su sample exhibits a slight peak at 340 nm. As pressure is induced, the peak centroid shifts to the right, until reaching 346 nm at 60 GPa.

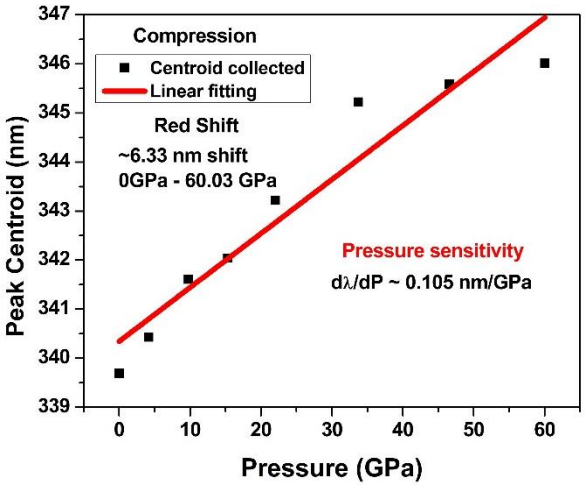

Fig. 71. Peak Centroid Change as Pressure Induced on PVDF Ce Su.

Fig. 71 depicts the peak centroid of PVDF Ce Su as pressure is induced. Before compression, the system centroid emits at 340 nm. As pressure is induced, the centroid shifts to higher nm. The system experiences a 6.33 nm shift from 0 to 60 GPa. As pressure is released, the system exhibits permanent luminescence deformation, staying at 346 nm.

Pressure (GPa)	x	y	N	Temperature (K)
0	0.172	0.003	0.874317	1976.26
3.01	0.172	0.003	0.874317	1976.26
8.32	0.172	0.003	0.874317	1976.26
14.51	0.172	0.003	0.874317	1976.26
22.75	0.172	0.003	0.874317	1976.26
35.07	0.172	0.003	0.874317	1976.26
47.52	0.172	0.003	0.874317	1976.26
62.40	0.172	0.003	0.874317	1976.26
Pressure released	0.172	0.003	0.874317	1976.26

Table 10: Luminescence Coordinates for PVDF Ce Su.

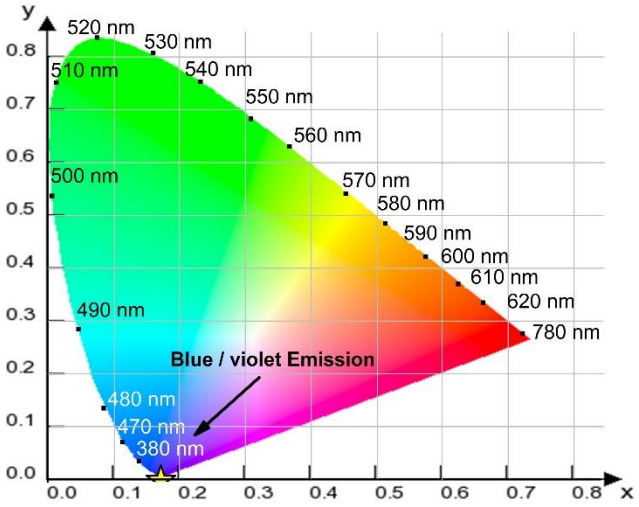

Fig. 72. Chromaticity Chart and Table for PVDF Ce Su.

The chromaticity chart portrays the luminescence color of PVDF Ce Su. The table shows the x and y coordinates as pressure is induced into the system. Before and after being compressed, PVDF Ce Su portrays a blue/violet luminescence. As the pressure is induced, the system depicted a slight change in luminescence.

The luminescence analysis verifies the creation of photo-mechanoluminescence polymeric based systems. The PVDF Eu Ni portrays the highest luminescence shift of the samples, exhibiting a shift from red luminescence to orange luminescence when under pressure.

PVDF Eu Su exhibits orange luminescence, and as pressure is added, the luminescence gets shifted into a higher orange color-spectrum. PVDF Ce Ni and PVDF Ce Su exhibit a change in their peak emission centroids, but the blue/violet luminescence color-spectrum shift is lower compared to the europium samples.

CHAPTER VI

CONCLUSION & FUTURE WORK

Fig. 73. PVDF-Lanthanide Flexible Fibers.

Lanthanide-doped polyvinylidene di-fluoride fibers were developed via the use of Forcespinning® technology. Europium and cerium elements were added into the polyvinylidene di-fluoride solution and magnetically-spun for 1 hour. The fibers diameters were in the micron range and contained luminescence properties. When a mechanical force was applied, the luminescence of such systems was altered.

As per our knowledge, this is the first-time photo-mechanoluminescent polymer systems have been made. The utilization of europium and cerium lanthanides produced the main source of luminescence on the photo-mechanoluminescent systems enhanced by the piezoelectricity properties of the PVDF. As pressure was induced on the system, there was a change in

luminescence. For instance, on polyvinylidene di-fluoride homogenized with 5% weight europium nitrate, the system portrayed red luminescence. The addition of 1.3 gigapascals shifted the color spectrum of the fiber system to orange, making an irreversible change in the light emission. The created photo-mechanoluminescent polymer systems could serve as potential optical-pressure sensors or monitoring systems.

The recommendations to optimize the findings of this project would be to decrease the fiber diameters into the nanometer range. This change could potentially improve the luminescence intensity of such systems. Also, the addition of other inorganic-lanthanide compounds could exhibit a different luminescence or color spectrum. Terbium or dysprosium could exhibit green or yellow luminescence without the addition of mechanical force. The addition of pressure could interact with the element's electronic transition and alter its luminescence.

REFERENCES

1. Chandra, B.P., V.K. Chandra, and P. Jha, Modelling of fracto-mechanoluminescence damage sensor for structures. Sensors and Actuators A: Physical, 2015. 230: p. 83-93.

2. Yacef, N., T. Bouden, and M. Grimes, Accurate ultrasonic measurement technique for crack sizing using envelope detection and differential evolution. NDT & E International, 2019. 102: p. 161-168.

3. Liu, P., et al., Fatigue crack detection using dual laser induced nonlinear ultrasonic modulation. Optics and Lasers in Engineering, 2018. 110: p. 420-430.

4. Bünzli, J.-C.G. and K.-L. Wong, Lanthanide mechanoluminescence. Journal of Rare Earths, 2018. 36(1): p. 1-41.

5. Chandra, B.P., Squeezing light out of crystals: Triboluminescence. Nuclear Tracks and Radiation Measurements (1982), 1985. 10(1): p. 225-241.

6. Arnold, E.K., Chemie Oberstufe. Cornelsen Schulverlage, 2015: p. 496-497.

7. Munson, C.A., et al., Chapter 10 - Laser-based Detection Methods of Explosives, in Counterterrorist Detection Techniques of Explosives, J. Yinon, Editor. 2007, Elsevier Science B.V.: Amsterdam. p. 279-321.

8. Martins, P., A.C. Lopes, and S. Lanceros-Mendez, Electroactive phases of poly(vinylidene fluoride): Determination, processing and applications. Progress in Polymer Science, 2014. 39(4): p. 683-706.

9. Thakur, P., et al., Role of Cerium (III)/Yttrium (III) nitrate hexahydrate salt on electroactive β phase nucleation and dielectric properties of poly(vinylidene fluoride) thin films. Vol. 5. 2015.

10. Garain, S., et al., Enhancement of Electroactive β-phase and Superior Dielectric Properties in Cerium Based Poly(vinylidene fluoride) Composite Films. Materials Today: Proceedings, 2018. 5(3, Part 3): p. 10084-10090.

11. Dandekar, M.P., et al., Photoluminescent electrospun europium complex Eu(TTA)3phen embedded polymer blends nanofibers. Optical Materials, 2018. 85: p. 483-490.

12. Xu, C.-N., et al., Development of Elastico-Luminescent Nanoparticles and their Applications. Vol. 45. 2006. 939-944.

13. Leverenz, H.W., An Introduction to Luminescence of Solids. 1968.

14. Atari, N.A., Piezoluminescence phenomenon. Physics Letters A, 1982. 90(1): p. 93-96.

15. Martin A. Lee, B.S., The Complete Social History of LSD: The CIA, the Sixties, and Beyond, in Acid Dreams. p. 174.

16. Reynolds, G.T., Piezoluminescence from a ferroelectric polymer and quartz. Journal of Luminescence, 1997. 75(4): p. 295-299.

17. Zink, J.I., Squeezing light out of crystals: Triboluminescence. Naturwissenschaften, 1981. 68(10): p. 507-512.

18. Fontenot, R.S., et al., Luminescent properties of lanthanide dibenzoylmethide triethylammonium compounds. Journal of Theoretical and Applied Physics, 2013. 7(1): p. 30.

19. Jha, P., et al., Ball impact induced elastico -mechanoluminescence for impact sensor. Vol. 195. 2017.

20. Leverenz, H.W., An introduction to luminescence of solids. 1950: Dover Publications.

21. Jackson, H.E. and L.M. Smith, Chapter Two - Optical Properties of Semiconductor Nanowires: Insights into Band Structure and Carrier Dynamics, in Semiconductors and Semimetals, S.A. Dayeh, A. Fontcuberta i Morral, and C. Jagadish, Editors. 2016, Elsevier. p. 17-74.

22. Harris, D.C., Quantitative Chemical analysis. W. H. Freeman and Company, 2006. 7th Edition.

23. Larkins, E.C. and J.S. Harris, 2 - Molecular Beam Epitaxy of High-Quality GaAs and AlGaAs, in Molecular Beam Epitaxy, R.F.C. Farrow, Editor. 1995, William Andrew Publishing: Park Ridge, NJ. p. 114-274.

24. Zhang, H. and Y. Fang, Temperature dependent photoluminescence of surfactant assisted electrochemically synthesized ZnSe nanostructures. Journal of Alloys and Compounds, 2019. 781: p. 201-208.

25. Kamimura, S., H. Yamada, and C.-N. Xu, Development of new elasticoluminescent material SrMg2(PO4)2:Eu. Journal of Luminescence, 2012. 132(2): p. 526-530.

26. Feng, A., Smet, and F. Philippe, A Review of Mechanoluminescence in Inorganic Solids: Compounds, Mechanisms, Models and Applications. Materials (Basel, Switzerland), 2018. 11(4): p. 484.

27. Runowski, M., et al., Optical Pressure Sensor Based on the Emission and Excitation Band Width (fwhm) and Luminescence Shift of Ce3+-Doped Fluorapatite—High-Pressure Sensing. ACS Applied Materials & Interfaces, 2019. 11(4): p. 4131-4138.

28. Skelton, E.F. and A.W. Webb, High-Pressure Research, in Encyclopedia of Physical Science and Technology (Third Edition), R.A. Meyers, Editor. 2003, Academic Press: New York. p. 345-363.

29. Sharipov, G.L., A.A. Tukhbatullin, and A.M. Abdrakhmanov, Triboluminescence of crystals and suspensions of inorganic salts of lanthanides. Protection of Metals and Physical Chemistry of Surfaces, 2011. 47(1): p. 13-19.

30. Akiyama, M., C.-N. Xu, and K. Nonaka, Intense Deformation Luminescence from Sintered Sr3Al2O6:Eu. Vol. 110. 2002. 1029-1031.

31. K. Chandra, V., B. Chandra, and P. Jha, Strong luminescence induced by elastic deformation of piezoelectric crystals. Vol. 102. 2013.

32. Akiyama, M., et al., Intense visible light emission from Sr3Al2O6:Eu,Dy. Vol. 73. 1998. 3046-3048.

33. Bispo-Jr, A.G., et al., Red-light-emitting polymer composite based on PVDF membranes and Europium phosphor using Buriti Oil as plasticizer. Materials Chemistry and Physics, 2018. 217: p. 160-167.

34. V. Bukvetskii, B., et al., Crystal structure and triboluminescence of centrosymmetric complex [Eu(NO3)3(HMPA)3]. Vol. 51. 2010. 1164-1169.

35. Yen, W.M., et al., Luminescence and Photoconductivity of Cerium Compounds. Vol. 90. 1996. 257-266.

36. Malyukin, Y., et al., Hydrogen peroxide sensing using Ce3+ luminescence of cerium oxide (CeO2-x) nanoparticles. Optical Materials, 2018. 85: p. 303-307.

37. Kaur, S., et al., Cerium luminescence in borate glass and effect of aluminium on blue green emission of cerium ions. Journal of Luminescence, 2013. 143: p. 31-37.

38. Ameen, I., et al., Luminescent, optical, magnetic and metamaterial behavior of cerium complexes. Journal of Saudi Chemical Society, 2019.

39. Vora, A., et al., Exchanging Ohmic Losses in Metamaterial Absorbers with Useful Optical Absorption for Photovoltaics. Scientific Reports, 2014. 4: p. 4901.

40. Adams, W., et al., Controlling optical absorption in metamaterial absorbers for plasmonic solar cells. SPIE Nanoscience + Engineering. Vol. 9546. 2015: SPIE.

41. Abdelaziz, M., Cerium (III) doping effects on optical and thermal properties of PVA films. Physica B: Condensed Matter, 2011. 406(6): p. 1300-1307.

42. Wu, L., et al., Power generation by PVDF-TrFE/graphene nanocomposite films. Composites Part B: Engineering, 2019. 164: p. 703-709.

43. Thakur, P., et al., Effect of in situ synthesized Fe2O3 and Co3O4 nanoparticles on electroactive β phase crystallization and dielectric properties of poly(vinylidene fluoride) thin films. Physical Chemistry Chemical Physics, 2015. 17(2): p. 1368-1378.

44. Ghafari, E. and N. Lu, Self-polarized electrospun polyvinylidene fluoride (PVDF) nanofiber for sensing applications. Composites Part B: Engineering, 2019. 160: p. 1-9.

45. Shirinov, A.V. and W.K. Schomburg, Pressure sensor from a PVDF film. Sensors and Actuators A: Physical, 2008. 142(1): p. 48-55.

46. Yokoyama, H., et al., Magneto-impedance properties of thin-film type sensors using CoNbZr/SiO2 multilayer films. Journal of Magnetism and Magnetic Materials, 2019. 478: p. 38-42.

47. Tang, E.L., L. Wang, and Y.F. Han, Space debris positioning based on two-dimensional PVDF piezoelectric film sensor. Advances in Space Research, 2019.

48. Liu, S. and D.H. Reneker, Droplet-jet shape parameters predict electrospun polymer nanofiber diameter. Polymer, 2019. 168: p. 155-158.

49. Zhang, X., et al., Enhanced and wavelength-tunable near-infrared luminescence from bismuth-doped silica thin films with Au nanocrystals. Journal of Alloys and Compounds, 2019. 772: p. 332-336.

50. Trefon-Radziejewska, D., et al., Thermophysical properties of methacrylic polymer films with guest-host and side-chain azobenzene. Materials Chemistry and Physics, 2019. 223: p. 700-707.

51. Flores, D., et al., Production of carbon fibers through Forcespinning® for use as anode materials in sodium ion batteries. Materials Science and Engineering: B, 2018. 236-237: p. 70-75.

52. Sarkar, K., et al., Electrospinning to Forcespinning™. Materials Today, 2010. 13(11): p. 12-14.

53. Savile Bradbury, B.J.F.a.O. (2019) Scanning electron microscope.

54. (2017) Scanning Electron Microscopy (SEM). Geochemical Instrumentation and Analysis.

55. Claesson, P.M., A. van der Wal, and A. Fogden, 8 - New Techniques for Optimization of Particulate Cleaning, in Handbook for Cleaning/Decontamination of Surfaces, I. Johansson and P. Somasundaran, Editors. 2007, Elsevier Science B.V.: Amsterdam. p. 885-927.

56. Stark, W. and W. Bohmeyer, 7 - Non-destructive evaluation (NDE) of composites: using ultrasound to monitor the curing of composites, in Non-Destructive Evaluation (NDE) of Polymer Matrix Composites, V.M. Karbhari, Editor. 2013, Woodhead Publishing. p. 136-181.

57. Mohamed, M.A., et al., Chapter 1 - Fourier Transform Infrared (FTIR) Spectroscopy, in Membrane Characterization, N. Hilal, et al., Editors. 2017, Elsevier. p. 3-29.

58. Torres, O., Lead Doped Carbon Nanofibers in Li-Ion Batteries, in Mechanical Engineering. 2019, The University of Texas Rio Grande Valley: Edinburg.

59. Gonzalez, H.G., Multifunctional Carbon Systems (Interlaminated Carbon Nanofiber Mats/ Carbon Nanotubes Polymer Composites), in Mechanical Engineering. 2019, The University of Texas Rio Grande Valley: Edinburg.

60. Li, Z., et al., Luminescence properties of SrBi2B2O7: Eu3+orange-red phosphor. Optik, 2018. 161: p. 38-43.

APPENDIX A

APPENDIX A

Table 1. State-of-the-Art Equipment

Equipment	Purpose	Results Obtained
Forcespinning(R) Cyclone	Fiber Production of PVDF-lanthanide systems	PVDF-Lanthanide fibers
Scanning Electron Microscope	Equipment required to take close image of fiber systems.	High resolution images of PVDF, PVDF Eu Ni, PVDF Eu Su, PVDF Ce Ni, PVDF Ce Su fibers. Results in Chapter 5.
Dynamic Scanning Calorimetry	Equipment used to check melting temperature, glass transition temperatures, and crystallinization degree of polymer systems.	Melting temperatures, crystallinity degree, and the alpha and beta pahses are obtained in the polymer lanthanide systems. Results in Chapter 5.
X-ray Photoelectron Spectroscopy	Verify polymer lanthanide systems chemical composition	The chemical composition was obtained. Results in Chapter 5.
Fourier Transform Infrared Spectroscopy	Analyze polymorph phases on the fiber systems	Alpha and Beta phase ratios were gotten. Beta relative phase was quantified. Results in Chapter 5
Photoluminescence Spectroscopy	Check luminescence of fiber systems	Luminescence was obtained from PVDF-lanthanide systems. Results in Chapter 5
Diamond Anvil Cell	Component to induce pressure on fiber systems	Luminescence change was recorded as pressure induced on systems. Results in Chapter 5

Table 2. State-of-the-Art software

Software	Purpose	Results Obtained
TA Analyzer	Analysis of DSC	Found crystallization degree, melting temperature, and glass transition temperatures on fiber samples. Result in Chapter 5
Avantage	Analysis of XPS	Found chemical composition of fiber samples. Results in Chapter 5
Zeiss smartSEM	Monitor image taking of SEM	High Resolution photos obtained of fiber samples. Results in Chapter 5
F980 software	Emission and excitation wave control on PL	Luminescence data of fiber samples. Results in Chapter 5
Origin 8	Graphing software to plot data	Plotted data as figures in thesis

BIOGRAPHICAL SKETCH

Carlos Hernandez, carlos_hdz1995@hotmail.com, was born in Reynosa, Tam., Mexico. He completed a Bachelor of Science in Mechanical Engineering at the University of Texas Rio Grande Valley in May 2017. During his undergrad years, he and a team of friends (Misael Martinez, Rodolfo Becerra, and Arnoldo Ventura) created a handwriting prototype to help people that suffer from Parkinson's disease write better. He was part of the Partnership for Research and Education in Materials Science (PREM), where he helped in the *Development and optimization of alumina fine fiber utilizing a centrifugal process*.

In the summer of 2017, he was accepted to the University of Texas Rio Grande Valley Mechanical Engineering Graduate Program, where he began working as a Graduate Research Assistant for Dr. Karen Lozano. During his time, he worked in projects such as the development of polyvinyl butyrate-polydiacetylene fibers for bacterial detection and the creation of polyvinylidene di-fluoride-lanthanide flexible systems for piezoelectric and luminescence applications. He completed and defended his thesis to attain his Master's degree in May 2019.